Strontium Isotope ($^{87}Sr/^{86}Sr$) Constraints on the Neoproterozoic Stratigraphy of the Northeastern Amadeus Basin, NT, Australia

Thesis submitted in accordance with the requirements of the University of Adelaide for an Honours Degree in Geology

Angus George Love

October 2017

THE UNIVERSITY of ADELAIDE

STRONTIUM ISOTOPE CONSTRAINTS ON THE NEOPROTEROZOIC STRATIGRAPHY OF NORTHEASTERN AMADEUS BASIN, NT, AUSTRALIA

RUNNING TITLE: STRONTIUM ISOTOPE CONSTRAINTS ON THE NEOPROTEROZOIC STRATIGRAPHYY OF THE AMADEUS BASIN

ABSTRACT

We measured elemental concentrations (including rare earth elements, REEs) and radiogenic strontium isotopes ($^{87}Sr/^{86}Sr$ ratios) from the Neoproterozoic carbonate-rich formations in the northeastern Amadeus Basin, in the central Australia. The acquired composite $^{87}Sr/^{86}Sr$ trend from the Amadeus Basin has the potential to be used for future strontium isotope stratigraphic (SIS) studies, in this semi-restricted intra-cratonic basin, as its local $^{87}Sr/^{86}Sr$ trend differs from the global Sr isotope seawater curve. Specifically, our composite $^{87}Sr/^{86}Sr$ trend from the Amadeus Basin is systematically more radiogenic compared to the coeval global ocean, which could be explained by a partial restriction of the Amadeus Basin during the Neoproterozoic. In particular, our elemental and isotope data show the following trends: the Ediacaran (post-Marinoan) Olympic cap carbonates (~635 Ma) revealed (i) radiogenic $^{87}Sr/^{86}Sr$ values which support the *meltwater plume* hypothesis and the above-mentioned basin restriction, and (ii) paleo-redox proxy data (Ce/Ce*) suggest more reducing (anoxic) conditions in the Amadeus Basin in the aftermath of the Marinoan glaciation. In contrast, the $^{87}Sr/^{86}Sr$ measurements of the Cryogenian Ringwood Member of the Aralka Formation (~658 Ma) revealed values that are approaching the global seawater $^{87}Sr/^{86}Sr$ curve, which in turn suggest relatively higher connectivity of the basin with the global ocean during this time. The paleo-redox proxy data (Ce/Ce*) from carbonates of the Cryogenian Ringwood Member and the Tonian Bitter Springs Group (~800 Ma) revealed less reducing and potentially sub-oxic conditions during these glacier-free intervals. Overall, our composite Neoproterozoic Sr isotope trend from the NE

Amadeus Basin seems to mimic the global seawater $^{87}Sr/^{86}Sr$ curve, however, with a systematic offset of about ~ 0.001 to ~ 0.002 units towards more radiogenic values.

KEYWORDS

Amadeus Basin, Neoproterozoic, Carbonates, Strontium Isotopes, Stratigraphy, Paleo-Redox

Table of Contents

LIST OF FIGURES AND TABLES

1. INTRODUCTION

Dating of Precambrian sedimentary carbonates is challenging due to the lack of index fossils compared to their Phanerozoic counterparts where one can rely also on biostratigraphy. The lack of fossils and higher potential for diagenetic resetting of radiogenic isotope systems, often hinders the application of traditional isotope systems used for conventional dating (Edwards et al., 2015). Strontium Isotope Stratigraphy (SIS) offers a solution for calibrating Precambrian sedimentary rocks through $^{87}Sr/^{86}Sr$ measurements of well-preserved marine carbonates. The Neoproterozoic Amadeus Basin in central Australia has numerous well-preserved carbonate rich sedimentary packages of presumably marine origins (Lindsay, 1987; Verdel and Campbell, 2017). The primary goal of this study is to use $^{87}Sr/^{86}Sr$ tracer in Neoproterozoic carbonates collected at selected sites in the north-eastern Amadeus Basin, along with other geochemical proxies (major and trace elements, including REEs), to better constrain; (i) the paleo-depositional environment (i.e., open marine versus restricted settings), and (ii) plausible stratigraphic position of selected carbonate strata collected in the basin. This study aims to generate a local Neoproterozoic $^{87}Sr/^{86}Sr$ reference curve for the Amadeus Basin, which in turn could be used as a reference 'baseline curve' for the intra-basin correlation and future detailed Sr isotope studies of sedimentary carbonates in the greater Amadeus Basin, NT (Northern Territory), Australia.

SIS relies on the fact that $^{87}Sr/^{86}Sr$ signature in the modern and ancient global oceans is expected to be homogenous due to the long residence time of Sr in seawater, which is typically on the order of more than ~1 Ma (Edwards et al., 2015). The Sr isotope budget of modern seawater, is a reflection of two major input fluxes of Sr derived from weathering of continental crust (~0.716) and hydrothermal inputs (~0.703; Edwards et al., 2015).

Thus, the change in the oceanic $^{87}Sr/^{86}Sr$ signature over geological time is a primarily function of the changing magnitudes of these Sr fluxes, which in turn indirectly reflect the tectonic

history of our planet. Throughout the Neoproterozoic era, the $^{87}Sr/^{86}Sr$ ratio of paleo-seawater has generally increased (Fig 1), and this trend has been attributed to the progressive increase in the radiogenic Sr sources to the coeval oceans due to enhanced weathering of continental crust (Halverson et al., 2007 and 2010; Cox et al., 2016).

1.1 Strontium Isotope Stratigraphy (SIS)

Temporal changes in the $^{87}Sr/^{86}Sr$ evolution of paleo-seawater over geological time can be used not only for the reconstruction of past changes in continental weathering versus hydrothermal fluxes, but also for determining the depositional age of marine carbonate sequences (with respect to global seawater $^{87}Sr/^{86}Sr$ reference curve, Fig 1) based on the well calibrated global $^{87}Sr/^{86}Sr$ seawater curve. Previous research of the temporal changes of the Sr isotope composition of paleo-seawater during the Neoproterozoic confirmed that the $^{87}Sr/^{86}Sr$ signature of the oceans was relatively stable and non-radiogenic with values of the order of ~0.7055 during the early Tonian, which is synchronous with the emplacement of coeval large igneous provinces (LIPs; Cox et al., 2016). The reconstructed $^{87}Sr/^{86}Sr$ trend of the Neoproterozoic oceans then exhibits a sharp rise to more radiogenic values of ~0.7075 during the late Tonian (from ~850 to 750 Ma), followed by a stable plateau around ~0.7070 between ~750 and 720 Ma (Cox et al. 2016; Kirschvink, 1992). This stable $^{87}Sr/^{86}Sr$ plateau then decreased to ~0.7064 just before the Sturtian Glaciation at the start of the Cryogenian. (see Fig 1). This sharp decrease in marine $^{87}Sr/^{86}Sr$ is believed to be a global phenomenon as it has been observed in data from the Mackenzie Mountains of NW Canada (Rooney et al., 2014), Svaalbard, as well as East Greenland (Cox et al., 2016). Finally, the Cryogenian interglacial (i.e., non-glacial interlude between Sturtian and Marinoan glaciations) is characterised by a stable rise in seawater $^{87}Sr/^{86}Sr$ to more radiogenic values of about 0.7073. Following the Marinoan glaciation (dated at ~640 to 635 Ma; Rooney et al., 2014), the Sr isotope data display

a gradual increase to ~0.7080, in the early Ediacaran, and subsequent increase to even more radiogenic values of about 0.7090 at the end of the Neoproterozoic. This last rise is thought to be due to Gondwana forming orogenies that provoked widespread continental weathering (Meredith et al. 2017; Collins & Pisarecsky, 2005). Importantly, previous studies suggested that the minor but systematic shifts to more radiogenic $^{87}Sr/^{86}Sr$ values observed in post-Marinoan cap carbonates (i.e., carbonates deposited in the aftermath of the Marinoan glaciation) reflect an enhanced continental weathering flux during rapid deglaciation in the aftermath of this 'Snowball Earth' event (Halverson et al., 2007; Liu et al., 2014; Phelps, 2015).

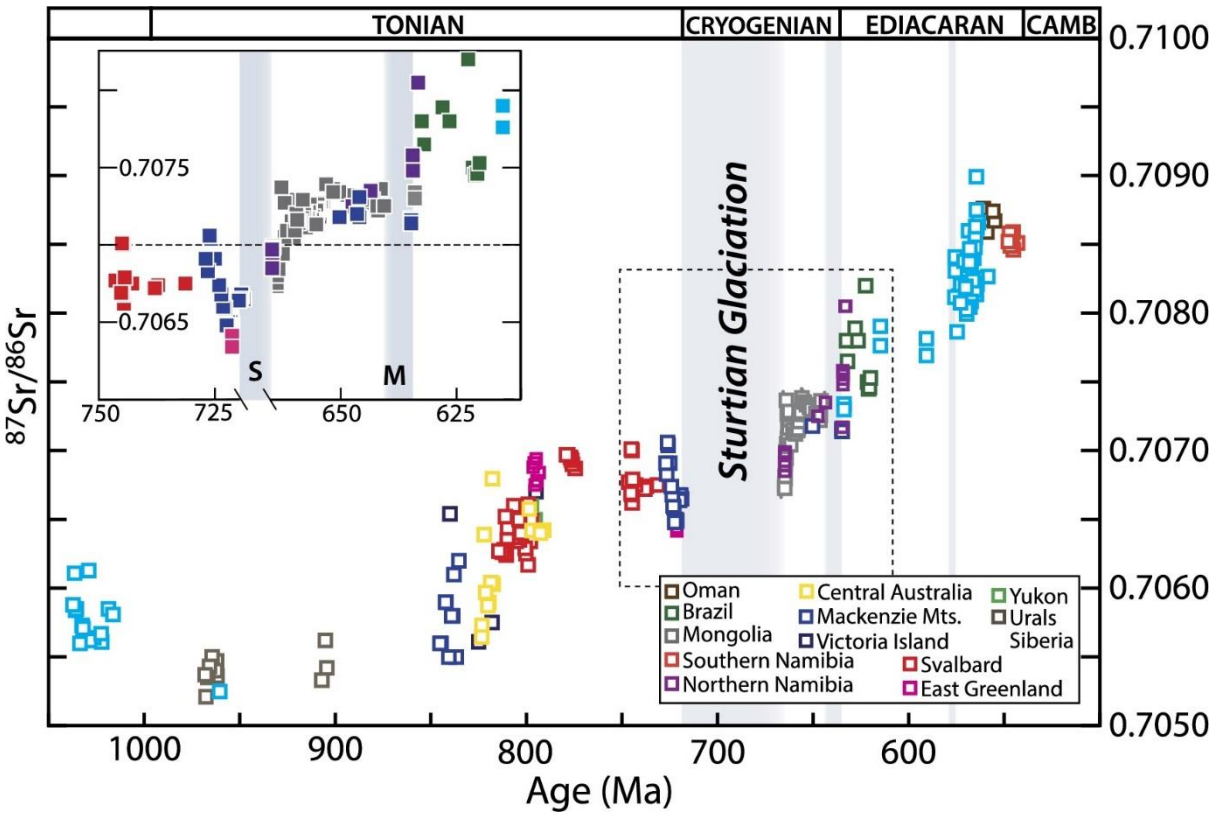

Figure 1: The Neoproterozoic $^{87}Sr/^{86}Sr$ global seawater curve after Cox et al. (2016). Adapted from previous studies of Halverson et al. 2007 and 2010. The inset displays the significant changes in seawater $^{87}Sr/^{86}Sr$ involving the Sturtain (S) and Marinoan (M) glaciations.

Apart from the application of SIS to the Neoproterozoic carbonate strata in the NE Amadeus Basin to refine the local stratigraphy, this study also aims to use the Sr isotope proxy

to further test the global character of the above post-glacial (i.e., post-Marinoan) weathering event by analysing $^{87}Sr/^{86}Sr$ in the Olympic cap carbonates from the NE Amadeus Basin. These results are then compared to published data from the coeval cap carbonates sampled on other paleo-continents and/or locations (Liu et al., 2014).

1.2 Sr Isotopes and 'Snowball Earth' event – Testing 'meltwater plume' hypothesis

This study aims to address an important question related to the origin of cap carbonates that formed in the aftermath of the Snowball Earth event (i.e., Marinoan Glaciation). Specifically, we use the $^{87}Sr/^{86}Sr$ proxy to further test the recently proposed *meltwater plume hypothesis* (Liu et al., 2014) as being the primary cause for the origin of post-Marinoan cap carbonates. Specifically, the latter hypothesis proposed that the precipitation of cap carbonates as being a consequence of the mixing between (i) freshwater from the post-glacial meltdown (with high $^{87}Sr/^{86}Sr$), and (ii) more dense and saline seawater (with low $^{87}Sr/^{86}Sr$) that was stored under the ice covered oceans.

Preliminary, although limited, results of Phelps and Verdel (2015) suggest that such radiogenic $^{87}Sr/^{86}Sr$ signals, possibly linked to the *meltwater plume,* might also be present in the equivalent post-Marinoan cap carbonates (i.e., Olympic Formation) in the Amadeus Basin, but more systematic and high-resolution studies are required to confirm this, which is one of the aims of this study. In addition, by comparing the $^{87}Sr/^{86}Sr$ data from cap carbonates in the Amadeus Basin, with the published radiogenic $^{87}Sr/^{86}Sr$ signals documented in the coeval post-Marinoan cap carbonates collected at other paleo-locations such as Flinders Rangers in SA and Mongolia (Liu, et al. 2014), we can evaluate the proposed existence of the presumably global *meltwater plume* in the Amadeus Basin. The latter represents a partially restricted intra-cratonic basin (Verdel and Campbell, 2017) and thus the purported radiogenic $^{87}Sr/^{86}Sr$ signal from the *meltwater plume* event, caused by the post-Marinoan deglaciation, is expected to be more

pronounced and detectable in the Amadeus Basin, compared to other paleo-locations (i.e., Flinders Ranges or Mongolia) where the continental processes and sources might be less dominant due to their different tectonic settings.

2. AMADEUS BASIN GEOLOGICAL SETTING AND BACKGROUND

The Amadeus Basin is an intra-cratonic sedimentary basin situated near Alice Springs in Central Australia (Fig 3), which consists of sedimentary sequences whose ages span from the Neoproterozoic to the late Paleozoic (Devonian), underlined by the Paleo- to Mid-Proterozoic basement (Fig 2). The Amadeus Basin, once a member of the Centralian Superbasin, was affected by the younger (i) Petermann Orogeny dated from ~600 to 540 Ma, causing uplift and accompanying thrusts, and also by (ii) the mid-Carboniferous tectonism (320 Ma) Alice Springs Orogeny (Walter et al, 1995). These events initiated the separation of the former Centralian Superbasin into the Amadeus, Officer, Georgina, Ngalia and Adelaide rift basins (Walter et al., 1995).

This study focuses on the Neoproterozoic sedimentary carbonates deposited in the northeastern Amadeus Basin. Specifically, we sampled and analysed the Tonian Bitter Springs Group, the Cryogenian Aralka Formation (Ringwood Member (RM)) and the Ediacaran Olympic Formation (i.e., post-Marinoan cap carbonate – Olympic cap), (for details see also Fig 2). The Cryogenian Aralka Formation, and Ediacaran Olympic Formation occur at critical times associated with the Marinoan glaciation and the so-called Snowball Earth event (Verdel and Campbell, 2017).

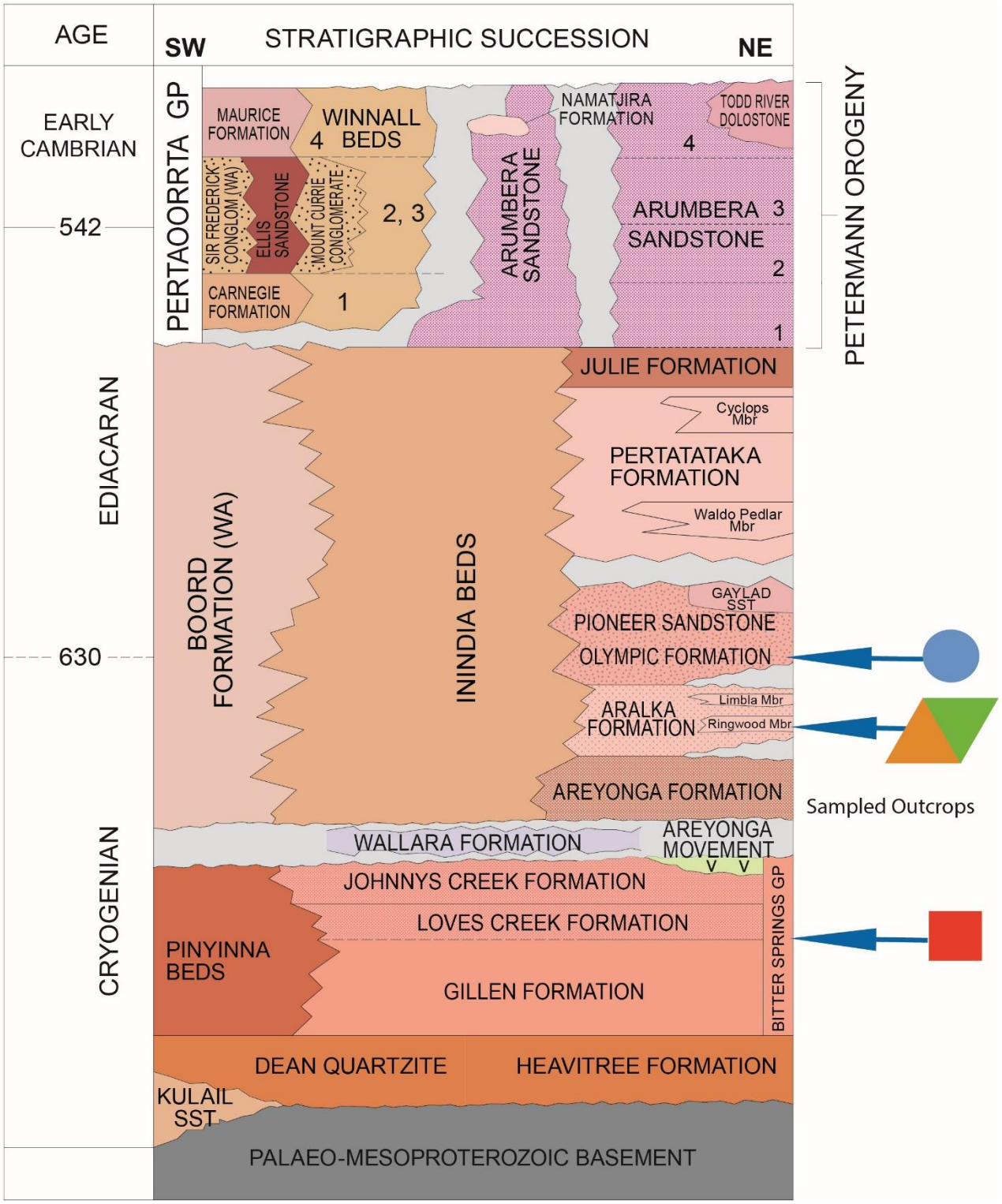

Figure 2: The Neoproterozoic/Cambrian stratigraphy and classification of sedimentary rocks in the greater Amadeus Basin. Blue arrows and colour symbols represent sedimentary rocks sampled for this project, and these include: the Bitter Springs Group, Ringwood Member of the Aralka Formation and the Olympic Formation (i.e., Olympic cap carbonate). Adapted from NTGS (Normington et al., in review).

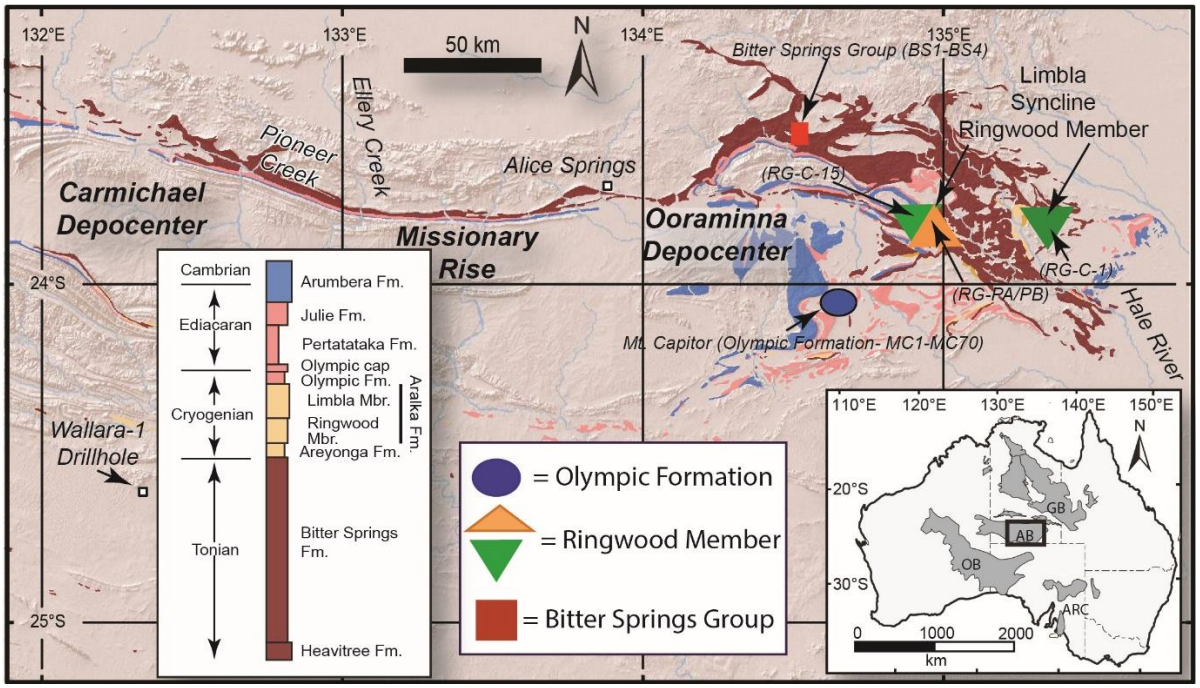

Figure 3: Northeastern region of the Amadeus Basin (AB), with occurrences of Neoproterozoic and Cambrian sedimentary rocks (after Verdel and Campbell, 2017), as well as our sampling sites (see circle, triangles and square symbols). The Limbla Syncline and Mt Capitor are areas where majority of the samples were collected (see appendix A for all GPS locations). The map of Australia (in the right lower corner) illustrates the occurrences of the other four large Neoproterozoic Basins (i.e., former Centralian Superbasin), including: Officers Basin (OB), Georgina Basin (GB), and ARC- (Adelaide Rift Complex).

2.1 Origin of Neoproterozoic Cap Carbonates and Snowball Earth Hypothesis

Kirschvink (1992) first proposed the concept of 'snowball earth' to explain the globally widespread and low-latitude glaciations in the Neoproterozoic, where subsequent subaerial volcanic outgassing is believed to be responsible for escaping the snowball earth conditions. The increase in atmospheric CO_2 eventually resulted in a rapid warming and deglaciation, which in turn caused flooding of shallow coastal areas and the precipitation of Ca-Mg rich carbonates (i.e., limestones and dolostones), producing the globally observed cap carbonate rocks (Hoffman et al. 1998).

The *meltwater plume* model predicts that these post-glacial cap carbonates formed relatively rapidly, i.e., within less than a few thousand years as a consequence of mixing between a low salinity meltwaters and more dense and saline seawaters (Shields, 2005). Liu et al. (2014) further developed this model, and proposed a *meltwater plume* whereby after

deglaciation a body of fresh and radiogenic waters (i.e., having high and non-marine $^{87}Sr/^{86}Sr$ signatures) sits on top of the coeval Neoproterozoic ocean waters (i.e., less radiogenic saltwater brine), where the mixing between these two contrasting water sources occurred within less than 10,000 years. Thus far, these presumably fresh and more radiogenic $^{87}Sr/^{86}Sr$ waters (i.e., *meltwater plume*) have been documented based on Sr isotope data from cap carbonates collected at sites in Mongolia (Ol cap dolostones) and South Australia (Nuccaleena cap dolostones in Flinders Ranges; (Liu et al. 2013; Liu et al. 2014)

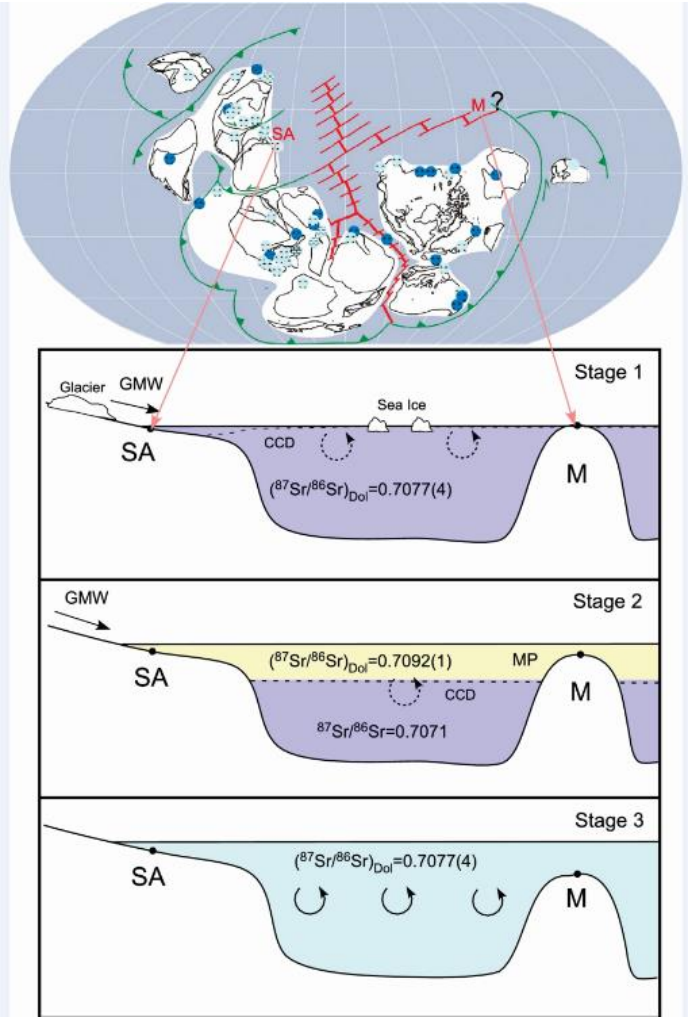

Figure 4: A schematic model for the post-snowball Earth *meltwater plume* hypothesis for the origin of cap carbonates, compared with the proposed $^{87}Sr/^{86}Sr$ signatures of the main water sources; modified after Liu (2014) based on data from the Flinders Ranges and Mongolia Cap carbonates. Where South Australia (SA); Mongolia (M); Glacial meltwater (GMW); Carbonate compensation depth. The light blue circles represent shallow marine deposits and dark blue circles represent deep marine deposits. Subduction zones and spreading ridges are shown. The location of Mongolia is unconstrained, but it is thought to be distant from Australia at the time.

Accordingly, obvious targets for further tests of the above *meltwater plume* hypothesis are at other correlative sites in Australia, and these include numerous shallow-water and presumably marine Neoproterozoic carbonates deposited in the Amadeus Basin (Kennedy, 1996). Preliminary Sr isotope data from Neoproterozoic carbonates sampled in the NE Amadeus Basin (Phelps & Verdel, 2015) indicate that the relatively best preserved carbonates which might be most suitable for follow up Sr isotope studies include: the Ringwood Member in the Aralka Formation, and potentially also the Olympic Formation or Olympic cap carbonates.

Apart from the above mentioned *meltwater plume* model (Fig. 4), there are several other hypotheses that have been put forward to explain the origin of the post-Marinoan cap carbonates (Shields et al, 2005; Liu et al. 2014). Specifically, three main hypothesis have been put forward to explain the global distribution and the specific isotope and geochemical patterns observed in the post-glacial cap carbonates, and these include: (i) an ocean overturn scenario involving an upwelling of deeper and alkalinity-charged waters (Shields, 2005), (ii) gas hydrate destabilisation (Kennedy, 1996), and (iii) the above *meltwater plume* model (Liu et al., 2014). Here we focus on the testing of the *meltwater plume* hypothesis through the application of Sr isotopes and trace elements proxies measured in the post-Marinoan cap carbonates from the northeastern Amadeus Basin (i.e., Mount Capitor region, see Fig, 3).

In particular, we aim to test whether the purported *meltwater plume* event in the Amadeus Basin, would be detectable as a pronounced radiogenic $^{87}Sr/^{86}Sr$ signature originating from the continentally derived freshwater/glacial water sources. This is expected because of the specific intra-cratonic tectonic settings of the Amadeus Basin, which is located more inland compared to the Flinders Ranges depositional system that was more connected with coeval open oceans (Verdel and Campbell, 2017). Thus, the purported deglacial *meltwater plume* carrying more radiogenic $^{87}Sr/^{86}Sr$ signatures is expected to be more distinct and pronounced

in the sedimentary record of the Amadeus Basin, as the latter was in closer proximity to the continental sources and glacially derived freshwater inputs with high $^{87}Sr/^{86}Sr$.

For this study, we collected samples from the northeastern Amadeus Basin, near Limbla Station (i.e., Ringwood Member of Arlka Formation carbonates (662.4 ± 4.6 Ma and 654.5 ± 3.8 Ma; Bold et al., 2016), and also near Mt. Capitor (i.e. sampling of Olympic Cap 635 Ma; Cox et al., 2016; Halverson, Dudás, Maloof, & Bowring, 2007).

2.2 Published $^{87}Sr/^{86}Sr$ records from the Neoproterozoic carbonates in Australia

Previous research demonstrated that most of the $^{87}Sr/^{86}Sr$ values measured in Australia's Neoproterozoic sedimentary carbonates are generally more radiogenic (Fig 5), compared to the expected Neoproterozoic global seawater $^{87}Sr/^{86}Sr$ curve (Fig 1, Cox et al., 2016).

Based on our understanding of the Sr isotope system in marine carbonates, there are at least three plausible explanations for these systematic enrichments in the radiogenic $^{87}Sr/^{86}Sr$ in the Australian Neoproterozoic carbonates, and these include: (i) diagenetic alteration by meteoric fluids (Kennedy, 1996), (ii) clay contamination of bulk carbonate $^{87}Sr/^{86}Sr$ signatures, and/or (iii) possible deposition of Australian Neoproterozoic carbonates in relatively more restricted marine environments (i.e., predominantly intra-cratonic basins) impacted by locally enhanced inputs of the radiogenic Sr from the continents.

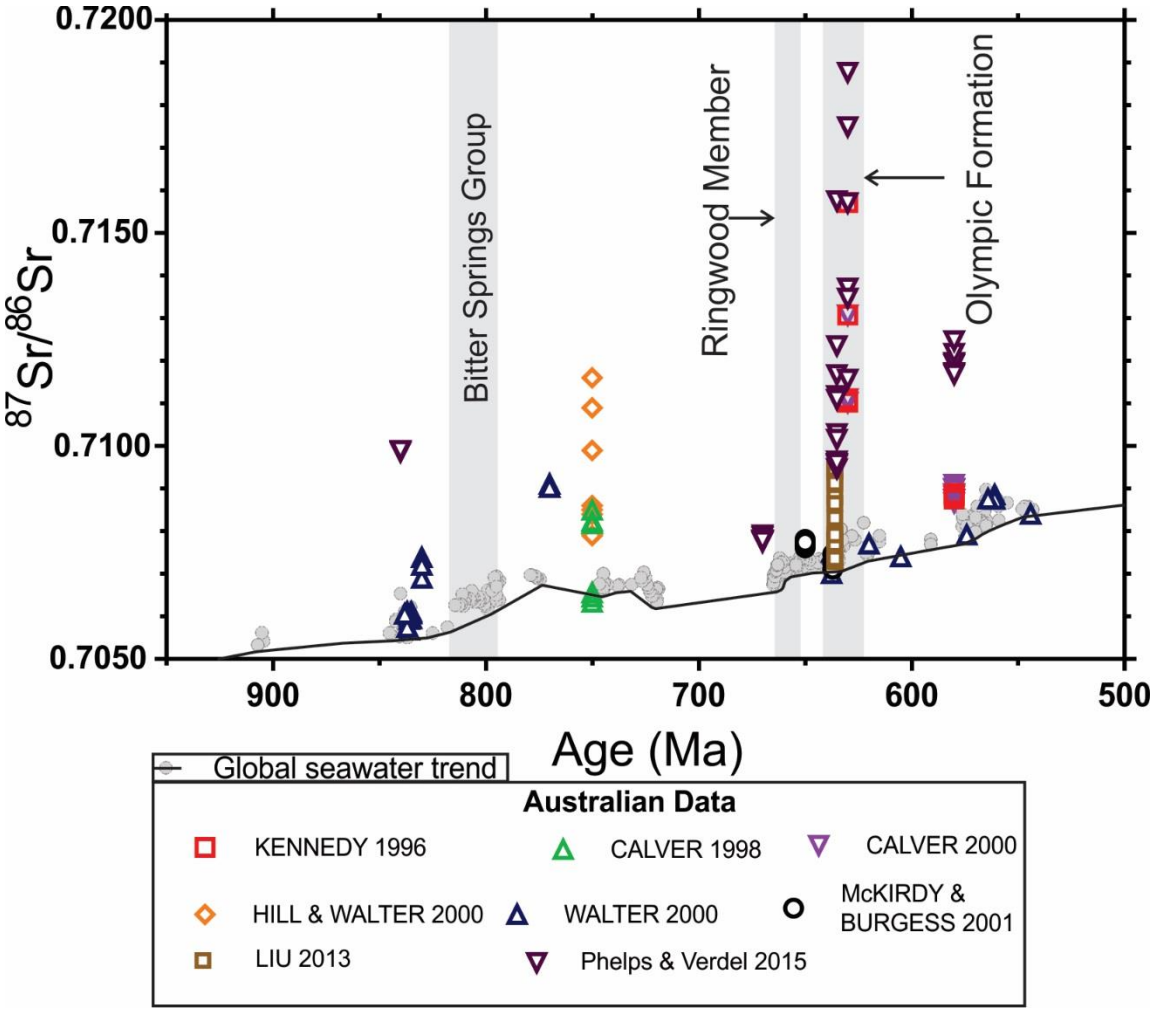

Figure 5: Global Sr isotope curve after Cox (2016) and other Australian Data from Kennedy 1996 (Amadeus Basin), Calver 1998 (Togari Group, Tasmania), Calver 2000 (Upper Burra Group, Adelaide Rift Complex), Hill_ Walter 2000 (Upper Burra Group, Adelaide Rift Complex), Walter 2000 (Bitter Springs Group, Amadeus Basin), Mckirdy_Burgess 2001(Brighton Limestone, Etina Formation), Liu 2013 (Nuccalena Formation, Adelaide Rift Complex), and Phelps 2015 (Olympic Formation, Amadeus Basin).

2.3 Introduction to Redox proxies in marine carbonates

The proposed *meltwater plume* scenario involves also a mixing of (i) relatively more oxic continental freshwater with high $^{87}Sr/^{86}Sr$, and (ii) deeper oceanic waters that are more saline and reducing with presumably lower $^{87}Sr/^{86}Sr$. Thus, the hypothesised *meltwater plume* model is expected to be reflected not only in the Sr isotope signatures of cap carbonates, but also in redox sensitive proxies such Ce/Ce* anomalies: $(Ce/Ce^*)_{SN} = Ce_{SN}/0.5(La_{SN} + Pr_{SN})$; after Bau and Dulski (1996). This is because the *meltwater plume* signal is expected to be more

oxic (or less reducing) due to the interactions of surficial waters with atmospheric oxygen (O_2), while the deeper and more saline seawaters are expected to be more reducing. The latter is anticipated because of the expected limited exchange between the ice-covered oceans and the atmospheric O_2, during the snowball earth events. Thus, if the *meltwater plume* model is indeed correct, we expect to see systematic changes in $^{87}Sr/^{86}Sr$ and Ce/Ce* proxies in cap carbonates as a consequence of mixing between (i) glacial *meltwater plume*, and (ii) coeval Marinoan paleo-seawater. The former with more radiogenic Sr isotopes and oxic signatures, while the latter with more reducing (i.e., more positive Ce/Ce*), and less radiogenic $^{87}Sr/^{86}Sr$ values.

3. METHODS

3.1. Study location and sampling sites

Carbonate samples for this study were collected from selected locations in the northeastern Amadeus Basin (see Fig 3, see appendix A for full GPS locations), based on the accessibility and geological mapping provided in for this area by previous studies (Phelps & Verdel, 2015). A total of 137 rock samples were collected, and of these, 113 were selected for trace element and REE analysis. Furthermore, 45 samples were selected for $^{87}Sr/^{86}Sr$ analysis, including the determination of key indicators for secondary and diagenetic processes such as: (i) the elemental Mn/Sr ratio as an index for meteoric diagenesis (Banner and Hanson, 1990), and (ii) the Al contents or Al/Ca ratios that are indicative of possible clay contamination of the primary marine carbonate-associated $^{87}Sr/^{86}Sr$ signatures.

3.2. Sample preparation

Samples were pre-screened to avoid any observed fractures or veins, and only micritic portions of samples were drilled and sampled for further geochemical and isotope studies. Powder (~50 mg) was drilled to yield the necessary amount of Sr for the isotope analysis. To

reduce the contamination by clays and detrital components that carry highly radiogenic Sr isotope signatures, all samples were leached sequentially, and the weight of powder was recorded before and after the leaching steps. We used a modified protocol based on Liu et al. (2014), where 50 mg of sample powder was leached for one hour in 1.8 ml of 1M ultra-pure ammonium acetate, ultrasonicated for 20 minutes, and then centrifuged for 10 minutes (3600 RPM). This first leachate was discarded as it contains mostly non-carbonate Sr associated with exchangeable sites of the clay fraction (Liu et al., 2014). The second step involves leaching with 1.8ml of 0.2M ultra-pure acetic acid (for one hour at room temperatures), ultrasonicated for 30 minutes, centrifuged for 10 minutes (3600 RPM). These leachates were also discarded, to minimise the impact of the clay-associated Sr fraction on measured $^{87}Sr/^{86}Sr$ values.

Finally, the remaining and rinsed carbonate-powder was leached (for one hour at room temperatures) in 1.8 ml of 0.5 M ultra-pure acetic acid, ultrasonicated for 30 minuted, centrifuged for 10 minutes (3600 RPM). These leached sample solutions (i.e., containing mostly carbonate-associated Sr) were then pipetted away and collected into separate teflon vials, and dried down. The dried down samples were then taken up in 5ml of 2% suprapure nitric acid (HNO_3), ready for the follow up analyses of elemental concentrations and Sr isotope compositions.

3.3. Elemental concentration analyses

The acid digested sample aliquots were prepared in two dilutions at 2,000 and 200,000 times for the elemental analyses with the ICP-MS Agilent 8900 (Inductively Coupled Plasma - Mass Spectrometer) at Adelaide Microscopy at the University of Adelaide. The analytical error for elemental concentrations was typically of the order of 3%, as determined by monitoring certified reference materials, including dolomites (JDo-1 dolomite standard).

3.4. Strontium isotope analyses ($^{87}Sr/^{86}Sr$) by TIMS

Samples of carbonates that yielded the highest Sr concentrations, within specific intervals (i.e., Ringwood Member of the Aralka Formation, and cap carbonates from the Olympic Formation), were selected for further Sr isotope analysis by thermal ionisation mass spectrometry (TIMS). Note that the Bitter Springs Group samples were not analysed for Sr isotopes, only for major and trace elements.

3.4.1. CHROMATOGRAPHIC PURIFICATION OF STRONTIUM

In order to measure the $^{87}Sr/^{86}Sr$ the pure Sr fraction must be separated from the sample matrix. The Sr fractions for the Ringwood Member (i.e., Sr-rich limestone samples) were purified using the semi-automated prepFAST-MC system, following the approach of Romaniello et al. (2015), (see also appendix B). The dolomitic samples (i.e., Olympic cap carbonates) required their Sr to be extracted through manual column chemistry using Sr-Spec resin, because of the lower Sr concentrations and high Ca and Mg contents in these samples (see also appendix B).

3.4.2. TIMS - ANAYLSES OF $^{87}SR/^{86}SR$

The purified Sr fractions were mixed with an activator or 'Bircks solution' and then loaded onto Re zone-refined filaments (for details see appendix B). High precision measurements were made using a multi-collector Phoenix TIMS instrument. The procedural standard of NBS SRM 987 yielded a long-term $^{87}Sr/^{86}Sr$ average of 0.710245 with 2 standard deviation of 0.000010, which agrees within the error with the recommended value of 0.710248. Total procedure Sr blanks for the prepFAST and Sr-Spec column chemistry were consistently below 100 ng of Sr, and thus negligible.

4. OBSERVATIONS AND RESULTS

In this section we present the basic description of the sampled carbonates and their measured geochemical data, including: $^{87}Sr/^{86}Sr$, Al/Ca, Mn/Sr ratios and REE's. Note that the geochemical data acquired from carbonates of the Aralka Formation (i.e., Ringwood Member) are plotted as two sub-groups: one to investigate shorter-term cyclic changes in $^{87}Sr/^{86}Sr$ within the parasequences of the Ringwood Member, and the other to document longer-term variations in Sr isotopes. The Bitter Springs Group was not analysed for strontium isotopes.

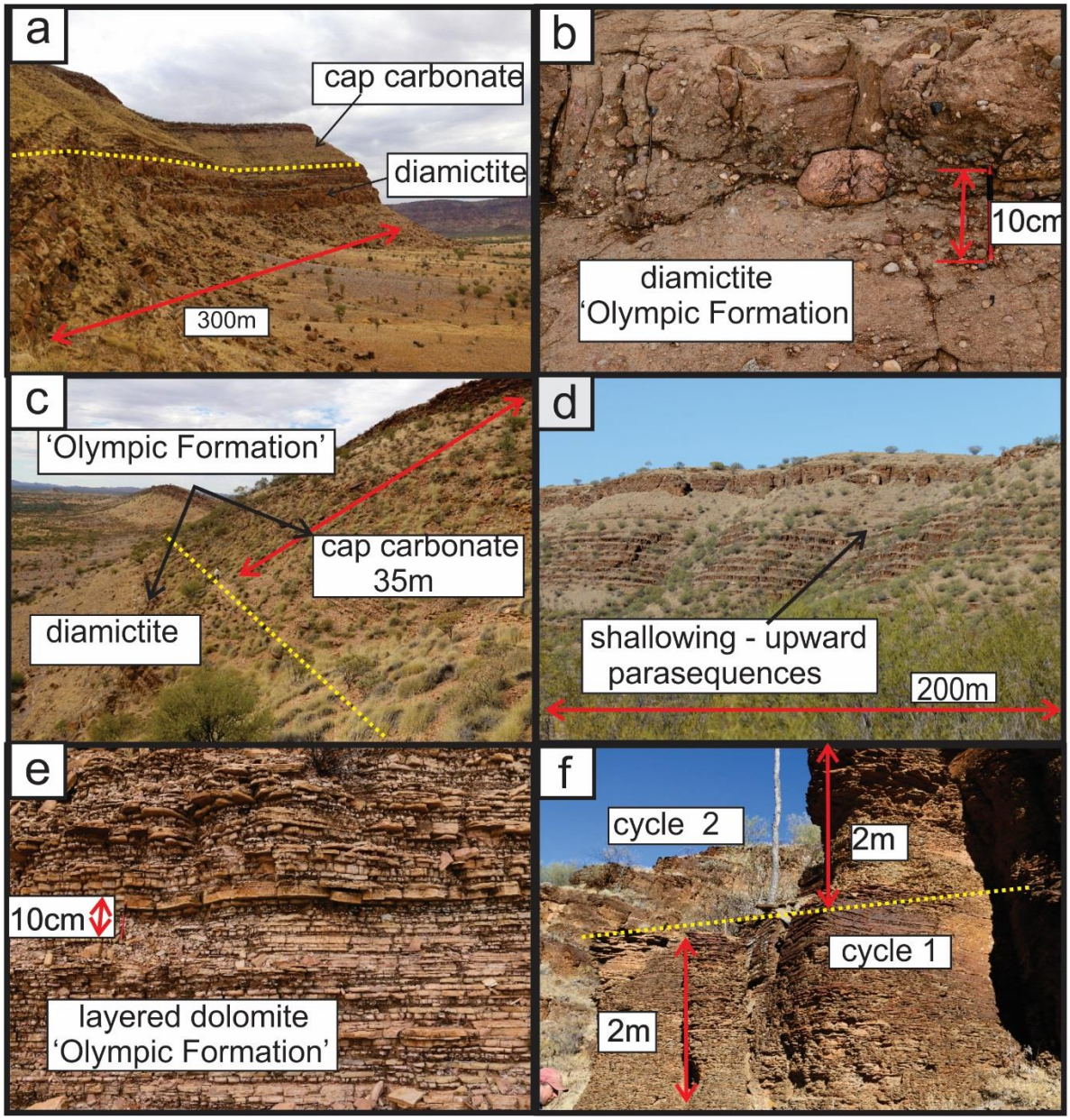

Figure 6: Field photographs from Amadeus Basin. (a) The full extent of the Olympic Formation Cap carbonate and the underlying diamictite. (b) Close-up image of the diamictite with dropstones. (c) The Olympic Formation with boundary between the diamictite and cap carbonate. (d) Shallowing upward parasequences of the Ringwood Member. (e) dolomitic layers of the Olympic cap carbonates. (f) Close-up image of the Ringwood Member parasquences.

4.2 Geochemical Results: Elemental and Isotope Compositions

Measured elemental ratios analysed in selected Neoproterozoic carbonates including: the Olympic Formation and the Ringwood Member, are listed in Table 1; and shown in Fig. 7, where we plot Mn/Sr and Al/Ca ratios against the corresponding $^{87}Sr/^{86}Sr$ measured in identical sample leachates. Using Mn/Sr and Al/Ca as indices for meteoric diagenesis and detrital clay contamination, respectively; our results suggest no obvious and statistically significant correlation between Mn/Sr and $^{87}Sr/^{86}Sr$ data (Fig. 7a, c). However, the results from Olympic cap dolomites and the Ringwood Member limestones revealed a strong and statistically significant ($p < 0.05$) correlation between the indices for detrital/clay contamination (Al/Ca ratios) and $^{87}Sr/^{86}Sr$ data (Fig. 7b, d).

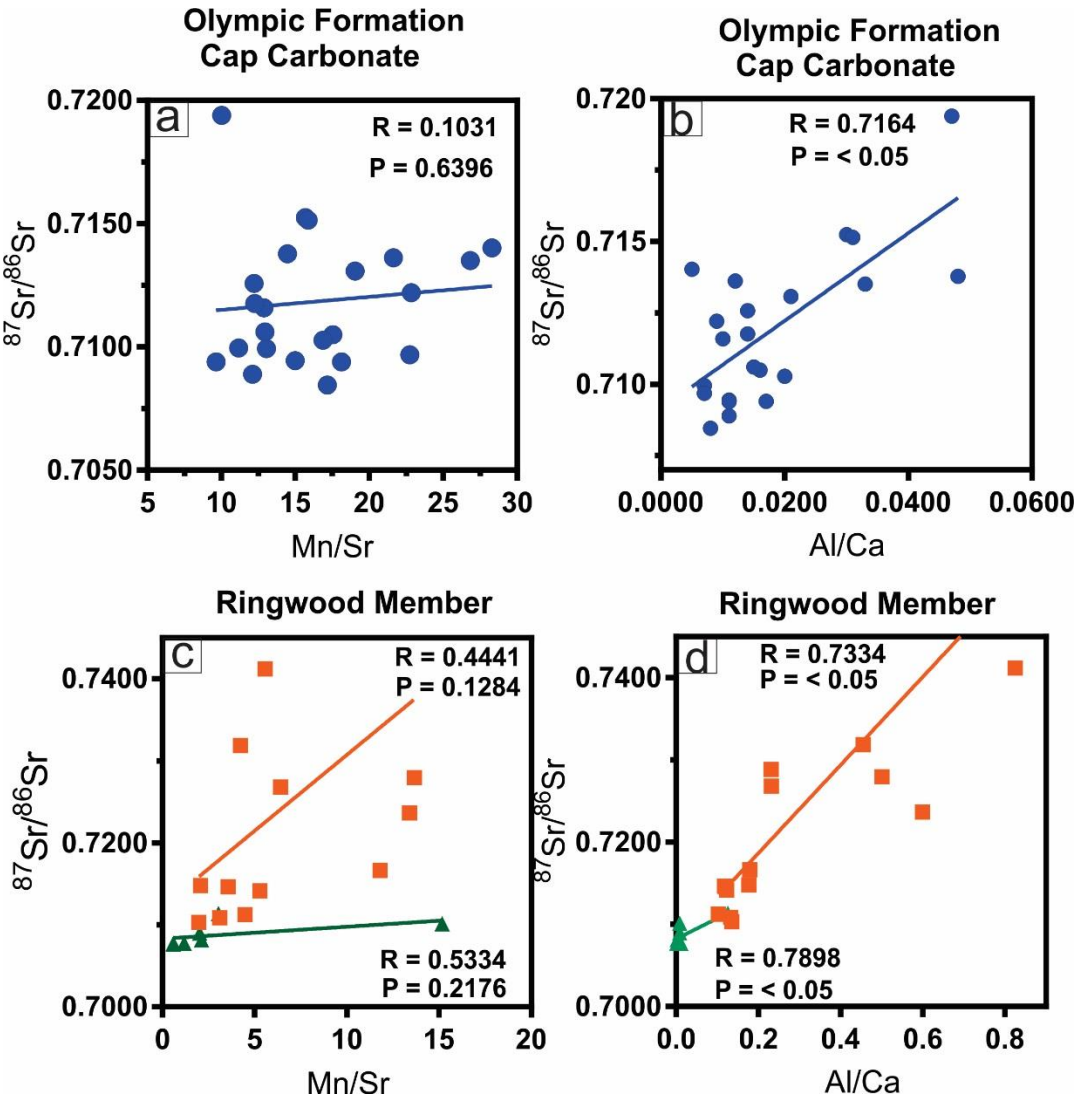

Figure 7: Trace element ratios of Mn/Sr and Al/Ca, as indices for the meteoric diagenesis and detrital contamination, plotted against $^{87}Sr/^{86}Sr$. Blue circles = Olympic Formation (Cap Carbonate), Orange Squares = Aralka Formation Parasequences (i.e., high-resolution sampling of the Ringwood Member – RM sedimentary cycles or parasequences), Green triangles = Aralka Formation (i.e., main transect through the entire Ringwood Member - RM).

4.3 $^{87}Sr/^{86}Sr$ as a function of stratigraphic height for the sampled sections

In Fig. 8, we plot the measured Sr isotope variations and Al/Ca ratios in the Olympic cap carbonates and the Ringwood Member limestones, which are plotted relative to their stratigraphic height, As to the Olympic cap carbonates, we observe a systematic decline in the $^{87}Sr/^{86}Sr$ ratio for the top ~5 metres of the studied section (see Fig. 8a). As to the Ringwood Member carbonates, we observe a tight coupling between $^{87}Sr/^{86}Sr$ and Al/Ca ratios, which is

documented for both the high-resolution parasequences (i.e., cycle 1 and 2, in Fig. 8e, f), but also for the entire section of the Ringwood Member carbonates (see Fig. 8c, d).

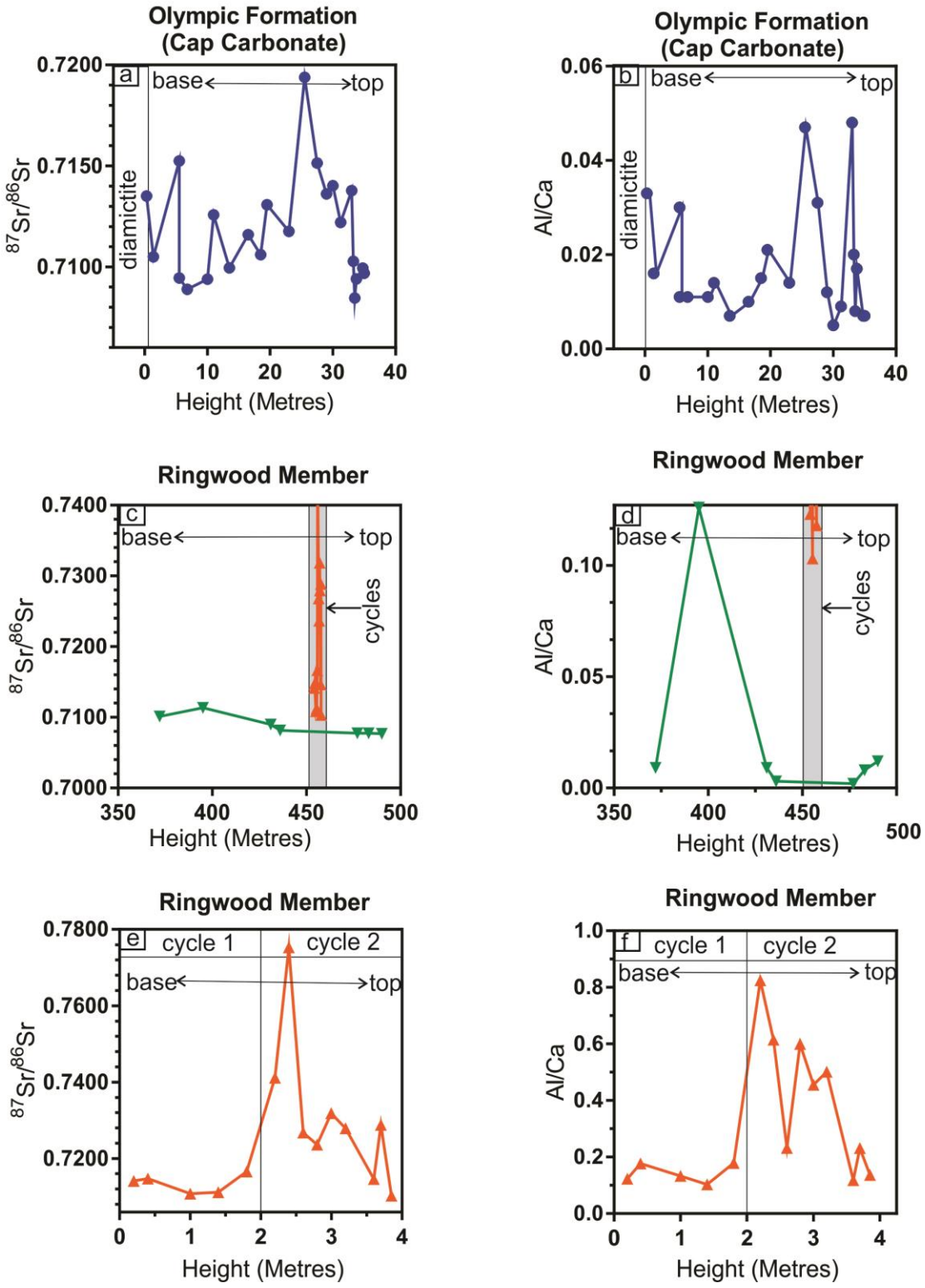

Figure 8: Measured $^{87}Sr/^{86}Sr$ and Al/Ca plotted against the relative stratigraphic height for the studied carbonates, including: (a) Olympic Formation (Cap Carbonate); (b) RG-C of Aralka Formation (RM = Ringwood Member); (c) RG-PA-PB of Aralka Formation (RM) and (d) Al/Ca across the Ringwood Member Parasequence (i.e., Cycle 1 and 2).

4.4 Results from Paleo-redox Proxies – Ce/Ce* Anomalies

Selected Rare Earth Elements (REEs) can provide valuable information on past redox conditions of seawater during the deposition of marine carbonates. As Ce is a redox sensitive REEs and as such its normalised values (Ce/Ce* anomalies) can be used as a paleo-redox proxy (for details see also information and equation in the Section 2.3). In addition, Pr is used to differentiate between possible positive La anomaly and a true negative Ce anomaly, based on the Ce/Ce* versus Pr/Pr* cross-plot (Fig. 9). Our REEs data and the calculated Ce anomalies are plotted in Fig. 9, which contains results from 113 carbonate samples analysed including: Olympic cap carbonates (dolostones and limestones), Ringwood Member carbonates (limestones), and Bitter Spring Group carbonates (i.e., dolostones). Overall, approximately 90% of the Olympic cap dolomite samples exhibit Ce/Ce* values that are in the positive anomaly zones, while results from the Ringwood Member and Bitter Springs Group carbonates yielded relatively less positive Ce/Ce* anomalies (Fig. 9).

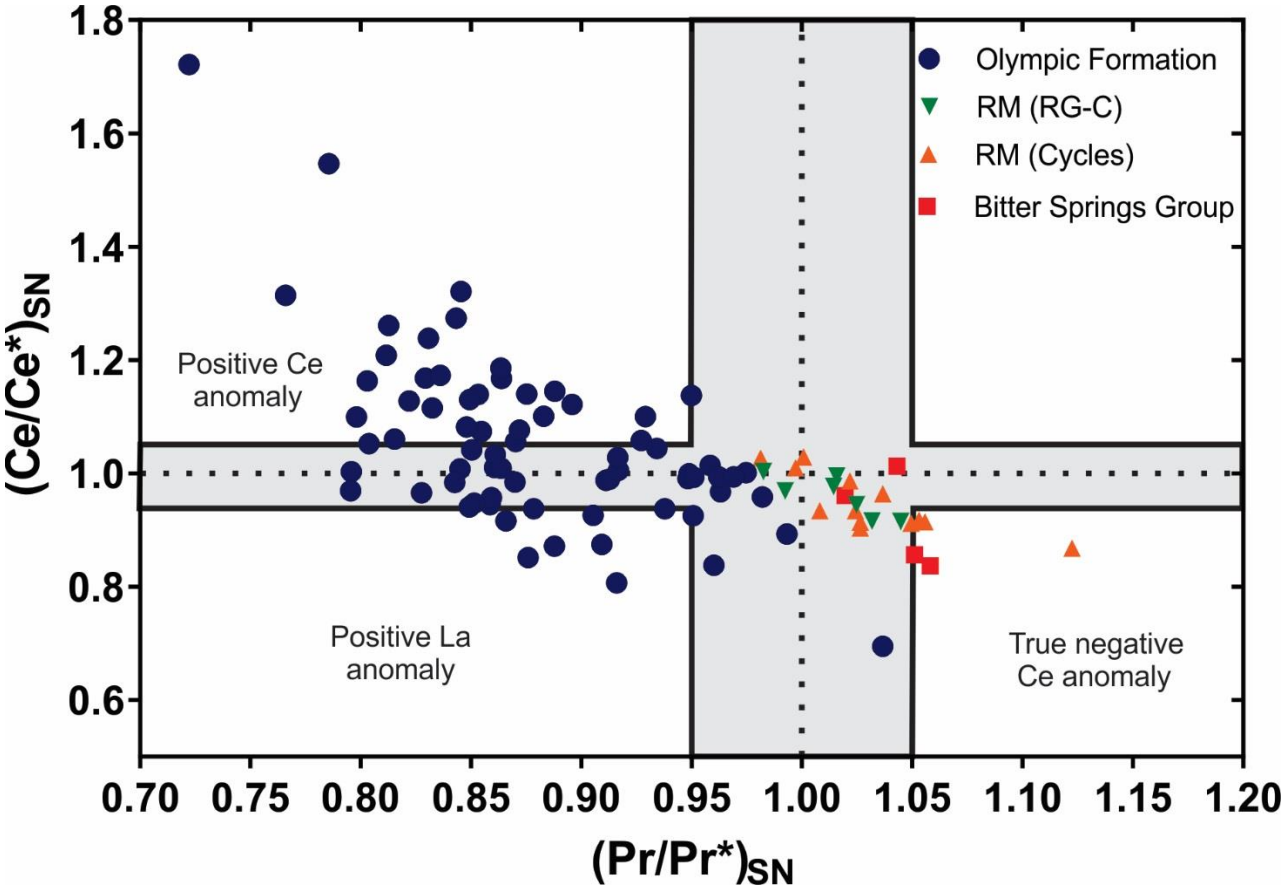

Figure 9: Shale normalised (SN) cross plot of Ce/Ce^*_{SN} and Pr/Pr^*_{SN} data from the studied Neoproterozoic carbonates from the Amadeus Basin (values calculated based on equations of Bau and Dulski, 1996); where $(Ce/Ce^*)_{SN} = Ce_{SN}/0.5[La_{SN} + Pr_{SN}]$, and $Pr^*_{SN} = Pr_{SN} = Pr_{SN}/0.5[Ce_{SN} + Nd_{SN}]$. Normalisation (SN) was after Nance and Taylor (1976) relative to Post Archean Australian Shale (PASS) (see appendix C for full data sets).

4.5 Geochemical summary table

Please see appendix C for full data sets.

Table 1: Measured $^{87}Sr/^{86}Sr$, Mn/Sr, Al/Ca ratios in selected Neoproterozoic carbonates from the NE Amadeus Basin, listed with respect to the relevant stratigraphic height of the sampled carbonates.

Sample ID	$^{87}Sr/^{86}Sr$	2SE	Mn/Sr (ppm/ppm)	Al/Ca (ppm/ppm)	Stratigraphic Height (meters)
Aralka Formation Parasequences (RM = Ringwood Member)					
RG-PA-2	0.714165	0.000002	5.277	0.123	0.2
RG-PA-3	0.714798	0.000003	2.063	0.177	0.4
RG-PA-6	0.710864	0.000003	3.107	0.133	1
RG-PA-8	0.711240	0.000003	4.486	0.103	1.4
RG-PA-10	0.716654	0.000007	11.803	0.179	1.8
RG-PB-2	0.741194	0.000005	5.571	0.825	2.2

RG-PB-3	0.775253	0.000005	11.296	0.615	2.4
RG-PB-4	0.726822	0.000003	6.409	0.232	2.6
RG-PB-5	0.723654	0.000004	13.387	0.600	2.8
RG-PB-6	0.731854	0.000003	4.223	0.455	3
RG-PB-7	0.727953	0.000003	13.662	0.501	3.2
RG-PB-9	0.714654	0.000008	3.556	0.118	3.6
RG-PB-10	0.728841	0.000003	149.083	0.231	3.7
RG-PB-11	0.710314	0.000003	1.966	0.136	3.85
RG-PA/PB 454 - 457.85m (stratigraphically to other RM samples)					
Aralka Formation (RM = Ringwood Member)					
RG-C-1	0.710132	0.000004	15.161	0.009	372
RG-C-6	0.711352	0.000003	3.047	0.126	395
RG-C-10	0.708977	0.000004	2.019	0.009	431
RG-C-12	0.708154	0.000003	2.121	0.003	436
RG-C-13	0.707739	0.000003	1.182	0.002	475
RG-C-14	0.707742	0.000003	0.599	0.008	476
RG-C-I5	0.707674	0.000003	0.602	0.012	477
Olympic Formation (Olympic Cap Carbonate; MC = Mount Capitor)					
MC-2	0.713505	0.000003	26.831	0.033	0.3
MC-4	0.710493	0.000004	17.543	0.016	1.4
MC-9	0.715243	0.000008	15.687	0.030	5.5
MC-10	0.709448	0.000003	14.998	0.011	5.5
MC-12A	0.708891	0.000008	12.102	0.011	6.8
MC-15	0.709390	0.000004	9.647	0.011	10
MC-17	0.712569	0.000069	12.220	0.014	11
MC-20B	0.709950	0.000022	11.181	0.007	13.5
MC-25	0.711590	0.000003	12.893	0.010	16.5
MC-30	0.710605	0.000003	12.945	0.015	18.5
MC-32	0.713074	0.000003	19.050	0.021	19.5
MC-39	0.711762	0.000003	12.259	0.014	23
MC-44	0.719392	0.000003	10.033	0.047	25.5
MC-48	0.715143	0.000003	15.869	0.031	27.5
MC-51	0.713612	0.000003	21.640	0.012	29
MC-53	0.714020	0.000004	28.290	0.005	30
MC-57	0.712200	0.000004	22.840	0.009	31.25
MC-62	0.713777	0.000003	14.464	0.048	33
MC-63	0.710273	0.000016	16.873	0.020	33.25
MC-64	0.708456	0.000003	17.170	0.008	33.5
MC-65	0.709395	0.000011	18.118	0.017	33.75
MC-69	0.709936	0.000006	13.056	0.007	34.75
MC-70	0.709677	0.000003	22.732	0.007	35

5. DISCUSSION

5.1. Criteria for evaluating meteoric diagenesis and clay contamination

For the purposes of the strontium isotope stratigraphy based on marine carbonates, it is critical that the samples of interest are well-preserved and their elemental and isotope compositions have not been affected by post-depositional processes, such as meteoric diagenesis and/or clay contamination. Diagenesis by meteoric waters can reset the original $^{87}Sr/^{86}Sr$ in marine carbonates, increasing their signatures to more radiogenic values while decreasing the Sr/Mn ratios in altered carbonates (Veizer et al. 1999; Banner and Hanson, 1990).

Based on these guidelines, well-preserved marine carbonates (i.e., limestones) should have low Mn/Sr (<0.1) and Rb/Sr (<0.1) ratios, and thus high Sr concentrations (>500 ppm; Cox et al. 2016). These trace element indices of diagenetic alteration can be thus used to reconstruct the true value of paleoseawater $^{87}Sr/^{86}Sr$ composition through geological time (Halverson et al., 2007). Generally, the least altered or best preserved marine carbonates are those with highest Sr contents, and lowest Al, and these typically also yield the lowest $^{87}Sr/^{86}Sr$ signatures, which are believed to best reflect the Sr isotope composition of the contemporary seawater. However, the studied Neoproterozoic carbonates from the Amadeus Basin have Mn/Sr ratios in excess of 0.1, and generally low Sr concentrations (with the exception of the Ringwood Member limestones), and therefore these samples would not necessarily meet the recommended criteria required for well-preserved samples. However, the generally higher Mn content in our carbonates might be also related to more reducing conditions of paleo-seawater in the Amadeus Basin rather than being a consequence of the meteoric diagenesis.

5.1.1 EVALUATION OF THE OLYMPIC FORMATION (CAP CARBONATE) DATA

The Sr isotopes data from the Olympic cap carbonates display a strong positive coupling with the indices for the clay contamination such as Al/Ca. Thus, despite a careful leaching of our samples to avoid clay contamination issues, it is obvious that the latter have affected the $^{87}Sr/^{86}Sr$ ratio measured in our samples of cap carbonates. In contrast, the lack of correlation between Sr isotopes and Mn/Sr data suggests that meteoric diagenesis was not the primary factor controlling the $^{87}Sr/^{86}Sr$ ratios in the Olympic cap carbonates; despite the extremely high Mn/Sr ratios (>30) observed in these samples.

5.1.2 EVALUATION OF THE RINGWOOD MEMBER DATA

Five samples yielded Mn/Sr ratios above 10, and one sample (RG-PB-10) has an extreme Mn/Sr value of 149, which suggest possible extensive diagenesis. Despite these indices from Mn/Sr ratios for meteoric diagenesis does not appear to have a dominant control on strontium isotopes in the Ringwood Member carbonates. However, the clay contamination indicator represented by Al/Ca appears to have a dominant and statistically significant (p-value < 0.05) control over the $^{87}Sr/^{86}Sr$ ratios in the studied carbonates.

5.2. Inferred primary Sr isotope signals in the Amadeus Basin

5.2.1 INTERPRETING THE PRIMARY SR ISOTOPE SIGNAL OF THE OLYMPIC FORMATION (POST-MARINOAN CAP CARBONATES)

All of the Olympic Formation $^{87}Sr/^{86}Sr$ ratios are considerably more radiogenic than the expected Neoproterozoic seawater. A statistically significant correlation occurs between Al/Ca and $^{87}Sr/^{86}Sr$ (see Fig 7.b, d), which indicates the role of clay contamination. As dissolved Al concentrations in seawater are expected to be very low, one might use the Al/Ca vs. $^{87}Sr/^{86}Sr$ relationship (see Fig. 7.b, d and Table 1) to infer the primary Sr isotope signature of paleo-seawater in the Amadeus Basin. Accordingly, the primary $^{87}Sr/^{86}Sr$ of paleo-seawater

could be estimated from a linear regression relationship between Sr isotopes and Al concentrations. Thus, the $^{87}Sr/^{86}Sr$ ratio corresponding to Al concentrations close to zero, is basically the Y-intercept $^{87}Sr/^{86}Sr$ value of about 0.7091 ± 0.0006 (see data in Fig. 10). Importantly, this value of 0.7091± 0.0006 is still much more radiogenic than the expected Marinoan paleo-seawater value of about 0.7077 (Liu et al. 2014). This observation, in turn, suggests that the Marinoan paleo-seawater $^{87}Sr/^{86}Sr$ signature in the Amadeus Basin was significantly more radiogenic compared to the coeval open ocean (see data in Cox et al. 2016). Interestingly, this intercept-derived $^{87}Sr/^{86}Sr$ value of paleo-seawater in the Amadeus Basin overlaps with the reconstructed Sr isotope signature for the post-Marinoan *meltwater plume* with the $^{87}Sr/^{86}Sr$ signature of ~0.7091 ± 0.0001 based on data from cap carbonates collected in Flinders Ranges and Mongolia (Liu et al., 2014).

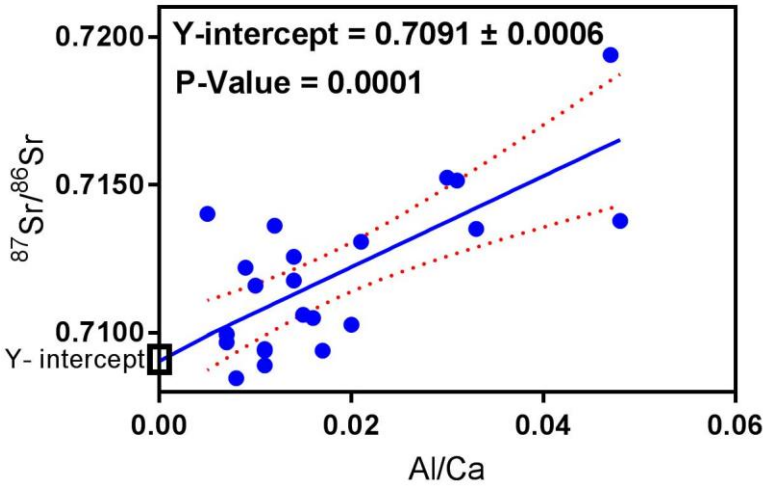

Figure 10: A cross-plot and linear regression of Al/Ca and $^{87}Sr/^{86}Sr$ data from the Olympic cap carbonates collected in the NT Amadeus Basin (Mount Capitor site). Note that the intercept $^{87}Sr/^{86}Sr$ value of 0.7091 corresponds to Al/Ca ratio of zero, indicating no or minimal effect of clay contamination on Sr isotope signatures.

5.2.1.1. STRONTIUM ISOTOPES IN THE OLYMPIC CAP CARBONATES FROM THE AMADEUS BASIN: IMPLICATIONS FOR THE MELTWATER PLUME HYPOTHESIS

The *meltwater plume* model of Liu et al. (2014), applied to the Nuccaleena cap dolomites from the Flinders Ranges, is directly relevant also to the coeval Olympic Formation cap carbonates (dolostones and limestones) deposited in the Amadeus Basin; as these two depositional systems are believed to be parts of the larger the Centralian Super Basin.

The model of Liu et al. (2014) proposes three main evolutionary stages for cap carbonate formation (Fig 4). At stage one, the $^{87}Sr/^{86}Sr$ of Nuccaleena cap dolomites is equivalent to the Marinoan paleo-seawater (see Fig. 11). In the second step (stage 2), the *meltwater plume* signal with more radiogenic $^{87}Sr/^{86}Sr$ becomes dominant. Finally, as the cap carbonate formation continues (stage 3), the *meltwater plume* becomes progressively mixed with the coeval ocean water and the $^{87}Sr/^{86}Sr$ of cap carbonates again approaches that of the Marinoan paleo-seawater (see Fig. 11).

Our data show that the situation was different for the Olympic Formation cap carbonates from the Amadeus Basin (Fig. 11), as $^{87}Sr/^{86}Sr$ in these samples is consistently more radiogenic compared to the paleo-seawater and overlaps with the purported Sr isotope signature of the *meltwater plume* (as determined based on data from Flinders Ranges and Mongolia). However, unlike at these sites where $^{87}Sr/^{86}Sr$ of cap carbonates approaches Marinoan paleo-seawater (see stages 1 and 3) this is not the case for the Amadeus Basin where $^{87}Sr/^{86}Sr$ data from the Olympic cap carbonates are systematically more radiogenic likely indicating a higher degree of restriction of this intra-cratonic basin with respect to the coeval global ocean.

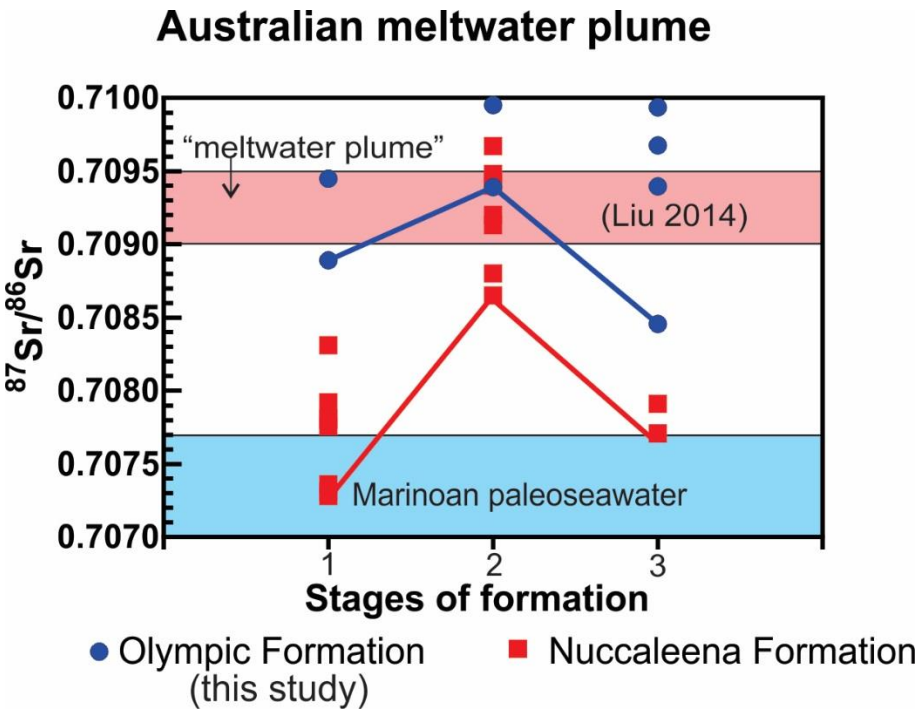

Figure 11: The compilation of $^{87}Sr/^{86}Sr$ data from cap carbonates in the Amadeus Basin (blue circles = this study) with other published data from Flinders Ranges (red squares, Liu et al., 2014). These cap carbonate Sr isotope trends (i.e., blue and red lines) are plotted along with the expected $^{87}Sr/^{86}Sr$ signature of the Marinoan paleo-seawater (blue rectangle) and the purported and more radiogenic fresh water plume (red rectangle). Note that numbers: 1, 2 and 3 correspond to three different stages during the freshwater plume scenario (for details see also Liu et al. 2014, or also Fig. 4).

5.1.2 STRONTIUM ISOTOPES IN RINGWOOD MEMBER AND IMPLICATIONS FOR PALEOSEAWATER

The Sr isotope signatures in the Ringwood Member parasequences are significantly affected by detrital clay contamination effects, as seen in the $^{87}Sr/^{86}Sr$ and Al/Ca data from these samples (Fig. 12c, d), plotted together with the expected Sr isotope composition of the coeval seawater. As more clay enters the cycles the measured $^{87}Sr/^{86}Sr$ of bulk carbonates become significantly more radiogenic, and also enriched in Al, despite the fact that a careful leaching procedure has been applied to minimise these effects.

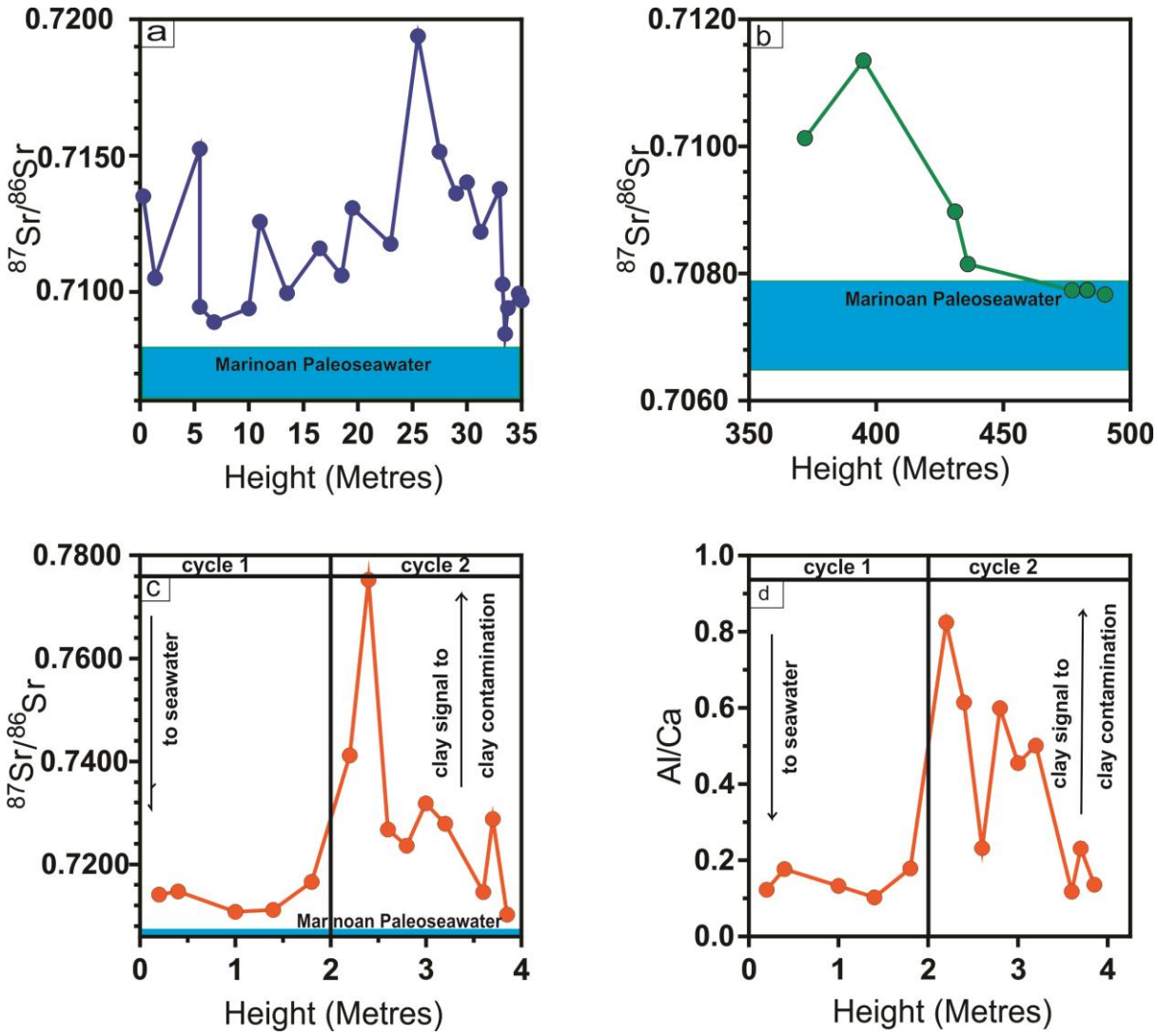

Figure 12: The Sr isotope variations in the Olympic cap carbonates (a), Ringwood Member (b) and its parasequences (c), and the Al/Ca ratios in the latter (d). The expected Marinoan paleo-seawater $^{87}Sr/^{86}Sr$ composition is plotted as well as a reference.

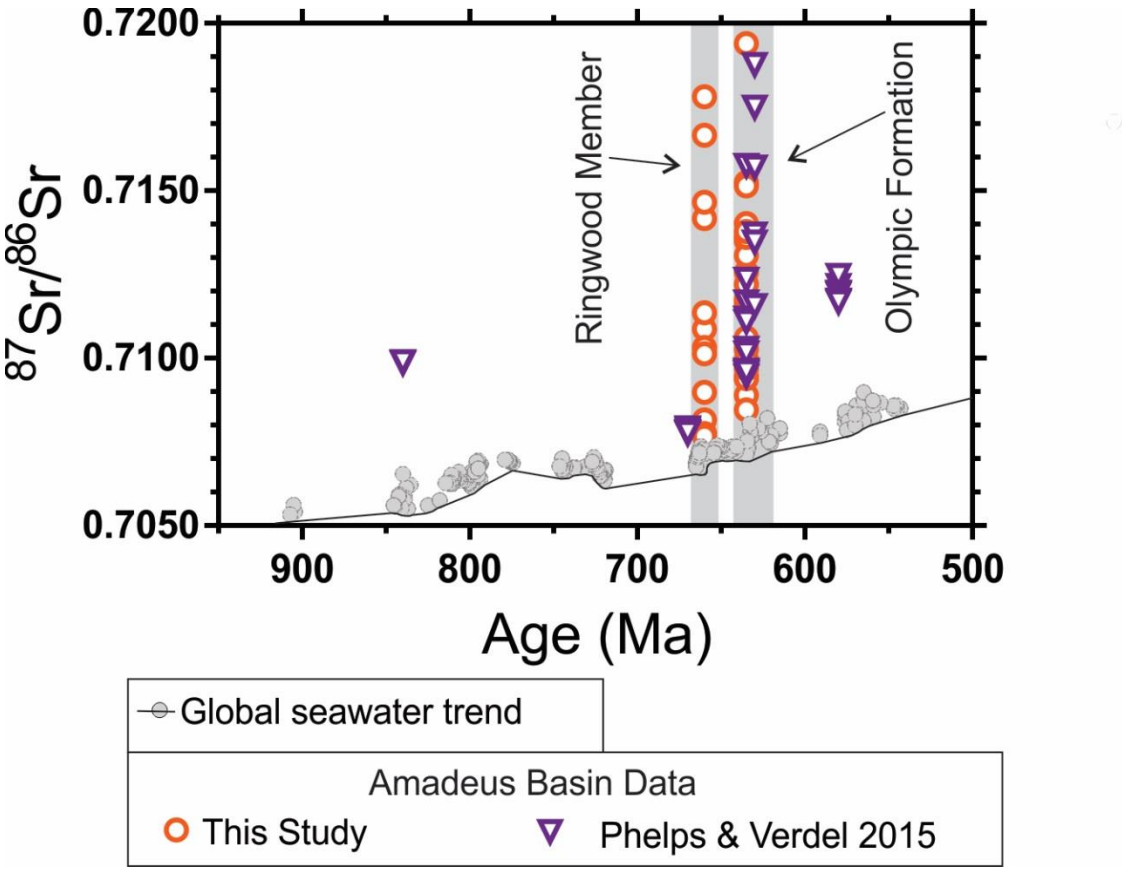

Figure 13: The complilation showing the global Neoproterozoic $^{87}Sr/^{86}Sr$ paleo-seawater curve (after Cox et al., 2016), along with the measured Sr isotope data from Neoproterozoic carbonates sampled in the NE Amadeus Basin (i.e., data from this study, and from Phelps and Verdel 2015).

The $^{87}Sr/^{86}Sr$ values obtained from this study are generally more radiogenic than the global Neoproterozoic $^{87}Sr/^{86}Sr$ paleo-seawater reference curve (see Fig. 13 and 16). However, four samples of limestones from the Ringwood Member: RG-C-12 (0.708154), RG-C-13 (0.707739), RG-C-14 (0.707742) and RG-C-15 (0.707674) yielded $^{87}Sr/^{86}Sr$ that are consistent and/or very close to the expected Neoproterozoic seawater Sr isotope signature. These results indicate that during the deposition of the Ringwood Member carbonates the NE part of the Amadeus Basin was connected and communicated with the open ocean. In contrast, the carbonates of the Olympic Formation yielded Sr isotope signatures that are all more radiogenic than the global paleo-seawater reference curve; nevertheless, a sample MC-64 (0.708456) yielded the least radiogenic $^{87}Sr/^{86}Sr$ that is approaching the global seawater values of about

0.7077 (Liu et al. 2014). Overall, our Sr isotope data from the Olympic cap carbonates indicate that during their deposition the NE Amadeus Basin was restricted from an open ocean and/or the radiogenic *meltwater plume* signal dominated the Sr isotope composition of local waters, and thus precipitated cap carbonates.

5.3 Paleo-Redox Conditions: Constraints from REEs and Ce/Ce* Proxies

Rare Earth Elements (REE's) patterns in seawater and marine carbonates provide valuable information of the redox conditions and paleo-depositional environments (Webb, Northdurft, Kamber, Kloprogge, & Zhao, 2009). Through understanding these systematic differences within REEs, especially the redox sensitive cerium (Ce) and europium (Eu) it is possible to constrain the paleo-redox conditions (i.e., oxic, sub-oxic, anoxic, euxinic) based on the REE analysis of carbonate rocks (Zhang et al. 2015).

Ce can exist in seawater in either Ce^{+3} or Ce^{+4} oxidation states, and the depletion of Ce concentrations in seawater occurs in the presence of oxygen, through the partial oxidation of Ce^{3+} to Ce^{4+} and its subsequent removal onto the surfaces of Mn and Fe oxides. Thus under typical oxic conditions, such as in modern surface oceans, the seawater and marine carbonate data exhibit a depletion in Ce concentrations, which in turn is reflected as a negative Ce/Ce* anomaly. In contrast, under anoxic condition, Ce is not removed from the water column and thus it behaves as other neighbouring REEs, and consequently exhibits no or positive Ce/Ce* anomaly (Hohl et al., 2017). La often mimics behaviour of neighbouring REEs, including Ce. This can produce false negative Ce anomalies, as such a method by Bau and Dulski (1996) is commonly used to define true negative Ce* anomalies through Pr/Pr* versus Ce/Ce* cross-plot divided into quadrants (see Fig. 14)

Compilation of our Ce/Ce* and Pr/Pr* data from Neoproterozoic carbonates from the NE Amadeus Basin show that the Olympic Formation (i.e., cap carbonates) exhibits a

systematic positive Ce* anomalies (Fig. 14), which could be interpreted in terms of anoxic conditions during the deposition of the Olympic cap carbonates. During this time of 'snowball earth' when oceans are expected to be covered by ice, it is anticipated that the coeval seawater would be potentially more reducing and depleted in O_2 due to a limited exchange of O_2 between the atmosphere and surface oceans.

Importantly, Ce/Ce* data from the Ringwood Member limestones (RG-C, and RG-PA/PB) and Bitter Springs Group carbonates show systematically more negative (or less positive) Ce/Ce* values, suggesting less reducing conditions in seawater and thus higher interactions of oceans waters with the atmospheric O_2. Thus, overall, our Ce/Ce* data indicate a progressive redox change in the Amadeus Basin during the Neoproterozoic, where conditions are more oxygenated (or rather less reducing) during the deposition of the Ringwood Member and Bitter Springs Group carbonates, but the situation changed to more reducing and anoxic conditions during the formation of the Olympic cap carbonates in the aftermath of the snowball earth event. However, overall the Ce/Ce* data from Neoproterozoic carbonates from the NE Amadeus Basin suggest that the redox conditions in the basin were mostly reducing and anoxic with possible transitions to less reducing or sub-oxic settings during the deposition of the Bitter Spring and/or Ringwood member carbonates.

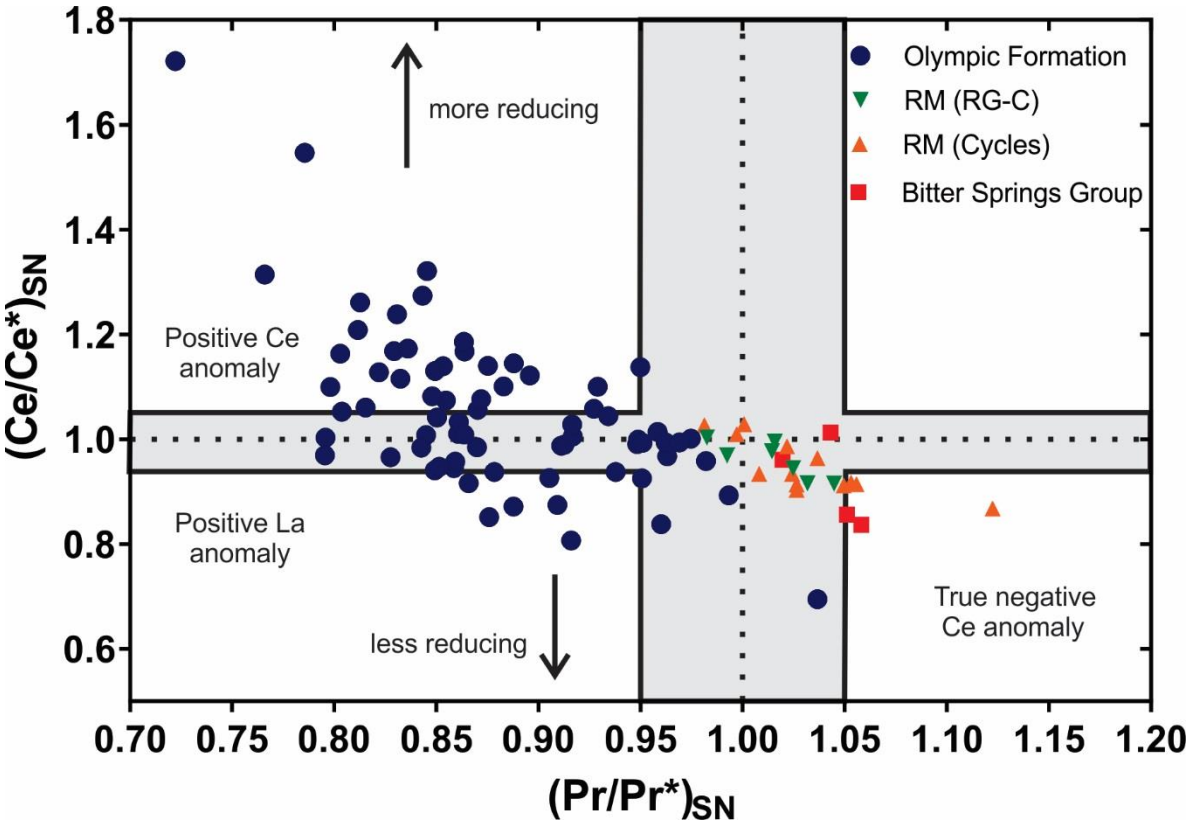

Figure 14: Shale normalised (SN-PAAS) cross plot of Ce/Ce*$_{SN}$ and Pr/Pr*$_{SN}$ data from the studied Neoproterozoic carbonates from the Amadeus Basin, and arrows showing conditions for more reducing (i.e., positive Ce/Ce* anomalies) and more oxidising (or less reducing) conditions, the later associate with negative Ce/Ce* anomalies.

5.3.1 PALEO-REDOX CONSTRAINTS ON OLYMPIC CAP CARBONATES

In Fig. 14, we observe that the majority of post-Marinoan cap carbonates collected at Mount Capitor plot in the positive Ce/Ce* anomaly area, suggesting anoxic and more reducing conditions during their deposition, and in fact not a single sample of studied cap carbonates plotted in the area of true negative Ce/Ce* anomaly. A detail view on the temporal changes in Ce/Ce* trend from the Olympic cap carbonates is available in Fig. 15a, which reveals more structure in this dataset when plotted as a function of stratigraphic height (in metres above the underlying glacial diamictite. Briefly, we observe a progressive increase in Ce/Ce* from the base of the section with values of about 0.9 to 1, to systematically more positive values of up to ~1.5 at the height of ca. 25 metres, and Ce/Ce* trend then rather abruptly decrease to values less than 1 (with a minimum up to about 0.7-0.8). These systematic changes during the

deposition of Olympic cap carbonates could be explained as progressive changes in redox conditions, where the waters are generally anoxic after the Marinoan glaciation, but the reducing conditions seems to intensify up the section (up to ca. 25 metres mark). This increasing anoxia could be related to a progressive flooding and thus deepening of the local depositional environment, which would then be dominated by more reducing and O_2 depleted deeper waters. The situation however changes in the top section where Ce/Ce* data suggest a sudden change in redox and less reducing condition, which by the way also coincide with shifts in $^{87}Sr/^{86}Sr$ to more marine values (see data in Fig. 12a). Thus is shift in redox could be related to the intrusion of fresh seawater into the basin, which was relatively less reducing.

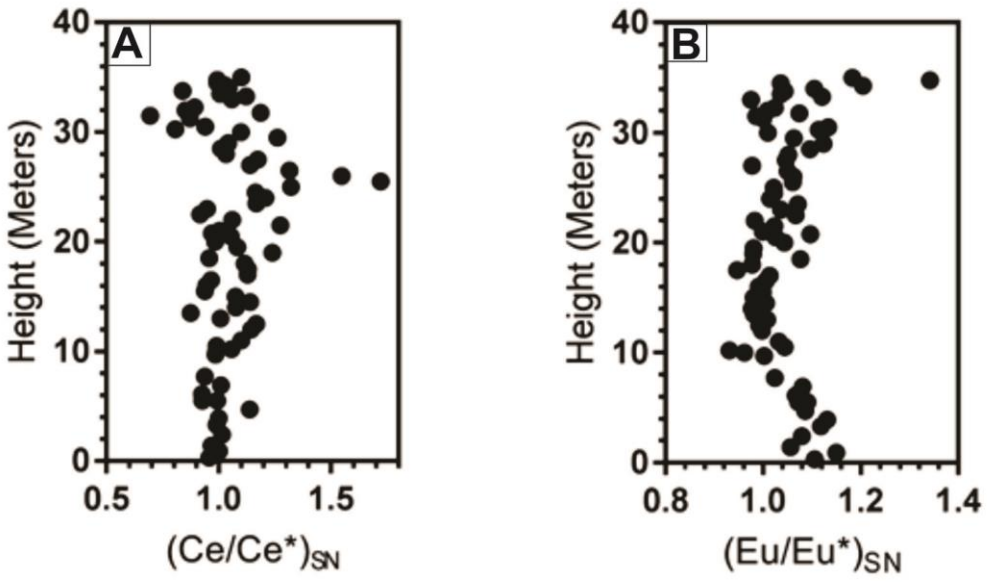

Figure 15: Ce/Ce^*_{SN} and Eu/Eu^*_{SN} trends of the Olympic Formation (cap carbonate profile from Mount Capitor), which are plotted as a function of stratigraphic height (from base to top).

In Fig. 15b, we also plot Eu/Eu* data which are typically used as proxies for hydrothermal fluxes into the oceans and/or possibly also for the weathering of feldspars as both these sources carry positive Eu/Eu* signatures. Considering the lack of correlation between Eu/Eu* and $^{87}Sr/^{86}Sr$ data in Olympic cap carbonates, which might point to possible hydrothermal inputs, we tentatively interpret the positive Eu/Eu* anomaly recorded just above

the glacial diamictite (i.e., within the first 10 meters of the section) to possibly reflect a signal from an enhanced weathering of feldspar sources at the continents associated with the post-snowball earth deglaciation event.

5.3.1 PALEO-REDOX CONSTRAINTS ON THE RINGWOOD AND BITTER SPRING CARBONATES

The Ringwood Member and Bitter Spring Group carbonates all plot systematically towards true negative Ce/Ce* anomaly area (Fig. 14), if compared to data from the Olympic cap carbonates, and thus we propose that the redox conditions during the deposition of these carbonates were relatively less reducing and possibly sub-oxic for some parts of the NE Amadeus Basin, especially for selected samples of Ringwood carbonates that yielded most negative Ce/Ce* data and close to marine $^{87}Sr/^{86}Sr$ values. As the Ringwood Member carbonates were deposited at times between two major glaciations (i.e., Sturtian and Marinoan) it is expected that during these 'ice-free' conditions the exchange and availability of atmospheric O_2 in seawater was higher (and thus conditions less reducing) compared to times when carbonates deposited in association with the major glaciations and/or in the aftermath of the snowball earth (i.e., the reducing condition during deposition of the Olympic cap carbonates).

5.5 Implications for the Meltwater Plume Model for Cap Carbonates Formation in the Amadeus Basin

The acquired Sr isotope and REEs data ($^{87}Sr/^{86}Sr$ and Ce/Ce* trends) from the Olympic cap carbonates are consistent with the proposed *meltwater plume* model (Liu et al., 2014), as our results indicate 'non-marine' and/or continent-derived (i.e., more radiogenic) Sr isotope signatures in the best-preserved and least contaminated cap carbonate samples. In addition, data from REEs also indicate a possible signal from weathered continental crust or feldspars, indicated by transient shift to more positive Eu/Eu* anomalies in the cap carbonates deposited just above the glacial diamictite. Importantly, redox-proxy data (Ce/Ce*) suggest a progressive deepening and more reducing conditions during the deposition of cap carbonates, indicating that the seawater in the Amadeus Basin as well as the purported *meltwater plume* might have been both quite reducing and O_2-depleted in terms of redox.

5.6 Local $^{87}Sr/^{86}Sr$ Isotope Curve for the Amadeus Basin: Implications for Basin Restriction and the Global Neoproterozoic Seawater Sr-Isotope Trend

Our results from the best preserved (i.e., least altered or clay contaminated) carbonate samples, with the lowest Al/Ca and Mn/Sr ratios, revealed that $^{87}Sr/^{86}Sr$ signatures in Neoproterozoic carbonates deposited in the NE Amadeus Basin are systematically more radiogenic compared to the estimated global Sr isotope composition of Neoproterozoic seawater (see the black versus red curves/trends in Fig. 16). This, in turn, suggests that during most of the Neoproterozoic the intra-cratonic Amadeus Basin was restricted from the coeval open ocean, as suggested by the systematic shift (on average about 0.001 to 0.002units) to higher $^{87}Sr/^{86}Sr$ values. These results suggest that the application of global seawater $^{87}Sr/^{86}Sr$ curve for stratigraphic purposes is of limited use for the Amadeus Basin, however, a local Sr isotope curve constructed for this basin would prove useful for future detailed studies and for chemostratigraphic uses.

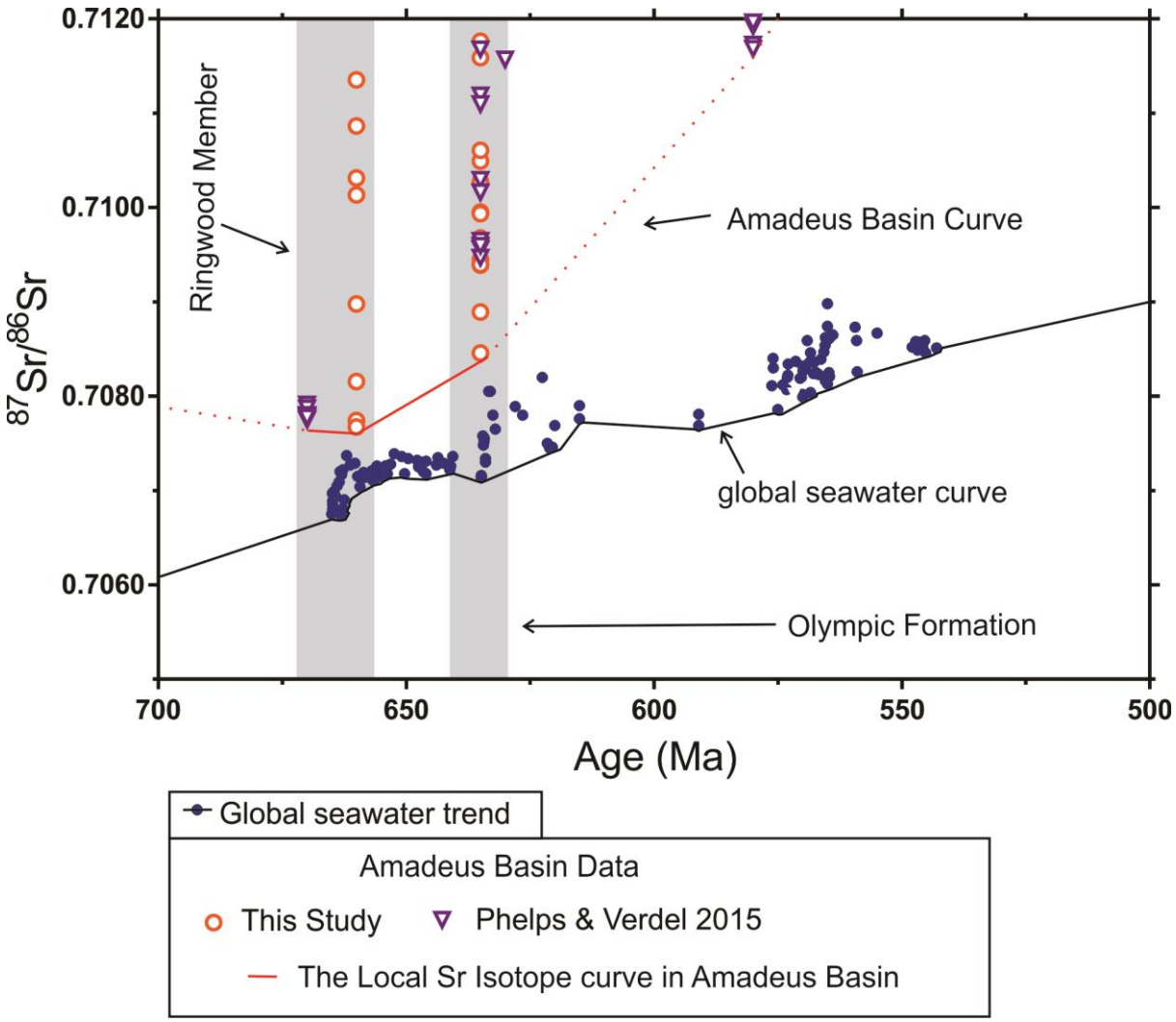

Figure 16: The global seawater trend compared to the current Amadeus Basin trend.

CONCLUSIONS

- The best-preserved Ediacaran (post-Marinoan) Olympic cap carbonates (~635 Ma) have more radiogenic $^{87}Sr/^{86}Sr$ values, compared to the coeval global seawater Sr isotope signatures, which thus support the proposed *meltwater plume* hypothesis for the origin of these cap carbonates, and our results also suggest relative restrictions of the NE Amadeus Basin during this time interval.

- The Cryogenian Ringwood Member carbonates of the Aralka Formation (~658 Ma) reveals $^{87}Sr/^{86}Sr$ values approaching the global seawater curve, which in turn infer relatively higher connectivity of the basin with the global ocean during this time..
- The paleo-redox proxy record based on Ce/Ce* reveals relatively less reducing (anoxic to sub-oxic) conditions present during the glacial-free periods of the deposition of the Ringwood Member and Bitter Springs Group carbonates. However, our data suggest that local redox conditions in the NE Amadeus Basin were more reducing (anoxic) in the aftermath of Marinoan glaciation during the deposition of the Olympic cap carbonates.
- Although, the local Amadeus Basin Sr-isotope curve during most of the Neoproterozoic (Cryogenian and lower Ediacaran) shows systematically more radiogenic values (about 0.001 to 0.002 units higher) compared to the global Neoproterozoic seawater $^{87}Sr/^{86}Sr$ curve, it can still be applied for future Sr-isotope stratigraphy studies and intra-basin correlations within the Amadeus Basin.

ACKNOWLEDGMENTS

I would like to acknowledge the NTGS for their outstanding support and funding for the project. In particular a special thanks to Dorothy Close, Christine Edgoose, Nigel Donnellan and Verity Normington from NTGS. A special thanks to Juraj Farkas, Charlie Verdel and Thomas Zack for convoying on the field trip. Thanks to supervisors Juraj Farkas, Charlie Verdel, Alan Collins and Grant Cox. A distinct thanks to David Bruce and Sarah Gilbert for their tireless assistance in clean lab and analytical work. Also thanks to lab assistance from Tony Hall, Mark Rollog, Robyn Williamson and Alec Walsh.

REFERENCES

BANNER, J. L., & HANSON, G. N. (1990). Calculation of simultaneous isotopic and trace element variations during water-rock interaction with applications to carbonate diagenesis. *Geochimica et Cosmochimica Acta, 54*(11), 3123-3137.

BAU, M., & DULSKI, P. (1996). Distribution of yttrium and rare-earth elements in the Penge and Kuruman iron-formations, Transvaal Supergroup, South Africa. *Precambrian Research, 79*(1), 37-55. doi: https://doi.org/10.1016/0301-9268(95)00087-9

CALVER, C. (1998). Isotope stratigraphy of the Neoproterozoic Togari Group, Tasmania. *Australian Journal of Earth Sciences, 45*(6), 865-874.

CALVER, C. R. (2000). Isotope stratigraphy of the Ediacarian (Neoproterozoic III) of the Adelaide Rift Complex, Australia, and the overprint of water column stratification. *Precambrian Research, 100*(1), 121-150.

COLLINS, A. S., & PISAREVSKY, S. A. (2005). Amalgamating eastern Gondwana: the evolution of the Circum-Indian Orogens. *Earth-Science Reviews, 71*(3), 229-270.

COX, G., HALVERSON, G. P., STEVENSON, R. K., VOKATY, M., POIRIER, A., KUNZMANN, M., & MACDONALD, F. A. (2016). Continental flood basalt weathering as a trigger for Neoproterozoic Snowball Earth. . *Earth and Planetary Science Letters*(446), 89-99. doi: DOI: 10.1016/j.epsl.2016.04.016

COX, G., JARRETT, A., EDWARDS, D., CROCKFORD, P. W., HALVERSON, G. P., COLLINS, A. S., . . . LI, Z.-X. (2016). Basin redox and primary productivity within the Mesoproterozoic Roper Seaway. *Chemical Geology, 440*(Supplement C), 101-114. doi: https://doi.org/10.1016/j.chemgeo.2016.06.025

EDWARDS, C. T., SALTZMAN, M. R., LESLIE, S. A., BERGSTRÖM, S. M., SEDLACEK, A. R., HOWARD, A., . . . YOUNG, S. A. (2015). Strontium isotope (87Sr/86Sr) stratigraphy of Ordovician bulk carbonate: Implications for preservation of primary seawater values. *Geological Society of America Bulletin, 127*(9-10), 1275-1289.

HALVERSON, G. P., DUDÁS, F. Ö., MALOOF, A. C., & BOWRING, S. A. (2007). Evolution of the 87 Sr/86 Sr composition of Neoproterozoic seawater. *Palaeogeography, Palaeoclimatology, Palaeoecology, 256*(3), 103-129. doi: 10.1016/j.palaeo.2007.02.028

HALVERSON, G. P., WADE, B. P., HURTGEN, M. T., & BAROVICH, K. M. (2010). Neoproterozoic chemostratigraphy. *Precambrian Research, 182*(4), 337-350. doi: https://doi.org/10.1016/j.precamres.2010.04.007

HILL, A. C., & WALTER, M. R. (2000). Mid-Neoproterozoic (~830–750 Ma) isotope stratigraphy of Australia and global correlation. *Precambrian Research, 100*(1), 181-211. doi: https://doi.org/10.1016/S0301-9268(99)00074-1

HOFFMAN, P. F., KAUFMAN, A. J., HALVERSON, G. P., & SCHRAG, D. P. (1998). A Neoproterozoic snowball earth. *Science, 281*(5381), 1342-1346. doi: 10.1126/science.281.5381.1342

KENNEDY, M. J. (1996). Stratigraphy, sedimentology, and isotopic geochemistry of Australian Neoproterozoic postglacial cap dolostones: deglaciation, d13C excursions, and carbonate precipitation. *Journal of sedimentary Research, 66*(6). doi: http://archives.datapages.com/data/sepm/journals/v66-67/data/066/066006/1050.htm?doi=10.1306%2FD42684A5-2B26-11D7-8648000102C1865D

KIRSCHVINK, J. L. (1992). Late Proterozoic low-latitude global glaciation: the snowball Earth. In J.W.Schopf (Ed.), *The Proterozoic Biosphere: A Multidisciplinary Study* (pp. 51-52): Cambridge University Press.

LINDSAY, J. F. (1987). Sequence stratigraphy and depositional controls in late Proterozoic-Early Cambrian sediments of Amadeus Basin, central Australia. *AAPG Bulletin, 71*(11), 1387-1403.

LIU, C., WANG, Z., & RAUB, T. D. (2013). Geochemical constraints on the origin of Marinoan cap dolostones from Nuccaleena Formation, South Australia. *Chemical Geology, 351*, 95-104. doi: 10.1016/j.chemgeo.2013.05.012

LIU, C., WANG, Z., RAUB, T. D., MACDONALD, F. A., & EVANS, D. A. D. (2014). Neoproterozoic cap-dolostone deposition in stratified glacial meltwater plume. *Earth and Planetary Science Letters, 404*, 22-32. doi: https://doi.org/10.1016/j.epsl.2014.06.039

MCKIRDY, D. M., BURGESS, J. M., LEMON, N. M., YU, X., COOPER, A. M., GOSTIN, V. A., . . . BOTH, R. A. (2001). A chemostratigraphic overview of the late Cryogenian interglacial sequence in the Adelaide Fold-Thrust Belt, South Australia. *Precambrian Research, 106*(1), 149-186. doi: https://doi.org/10.1016/S0301-9268(00)00130-3

MEREDITH,W., HOSHINO, Y., POSHIBAEVA, A., SNAPE, C., POSHIBAEV, V., VERSTEEGH, G. J., . . . NEUMANN, M. (2017). Cryogenian evolution of stigmasteroid biosynthesis. *Science Advances, 3*(9), e1700887.

NORMINGTON, V. Revised stratigraphy of drillholes CPDD001, CPDD002 and CPDD003, Pipeline Prospect, northeast Amadeus Basin. *Northern Territory Geological Survey, Technical Note.*

PHELPS, B., & VERDEL, C. (2015). *Strontium isotope and trace element constraints on Neoproterozoic carbonates in the Amadeus Basin, central Australia.* (BSc (Honours)), The University of Queensland

Unpublished.

ROMANIELLO, S., FIELD, M., SMITH, H., GORDON, G., KIM, M., & ANBAR, A. (2015). Fully automated chromatographic purification of Sr and Ca for isotopic analysis. *Journal of Analytical Atomic Spectrometry*, *30*(9), 1906-1912.

ROONEY, A. D., MACDONALD, F. A., STRAUSS, J. V., DUDÁS, F. Ö., HALLMANN, C., & SELBY, D. (2014). Re-Os geochronology and coupled Os-Sr isotope constraints on the Sturtian snowball Earth. *Proceedings of the National Academy of Sciences*, *111*(1), 51-56.

SHIELDS, G. A. (2005). Neoproterozoic cap carbonates: a critical appraisal of existing models and the plumeworld hypothesis. *Terra Nova*, *17*(4), 299-310. doi: 10.1111/j.1365-3121.2005.00638.x

VERDEL, C., & CAMPBELL, M. (2017). Neoproterozoic carbon isotope stratigraphy of the Amadeus Basin, central Australia. *GSA Bulletin*, *129*(9-10), 1280-1299.

WALTER, M., VEEVERS, J., CALVER, C., GORJAN, P., & HILL, A. (2000). Dating the 840–544 Ma Neoproterozoic interval by isotopes of strontium, carbon, and sulfur in seawater, and some interpretative models. *Precambrian Research*, *100*(1), 371-433.

WALTER, M., VEEVERS, J., CALVER, C., & GREY, K. (1995). Neoproterozoic stratigraphy of the centralian superbasin, Australia. *Precambrian Research*, *73*(1-4), 173-195.

APPENDIX A: GPS LOCATIONS AND MAP OF SAMPLE SITES

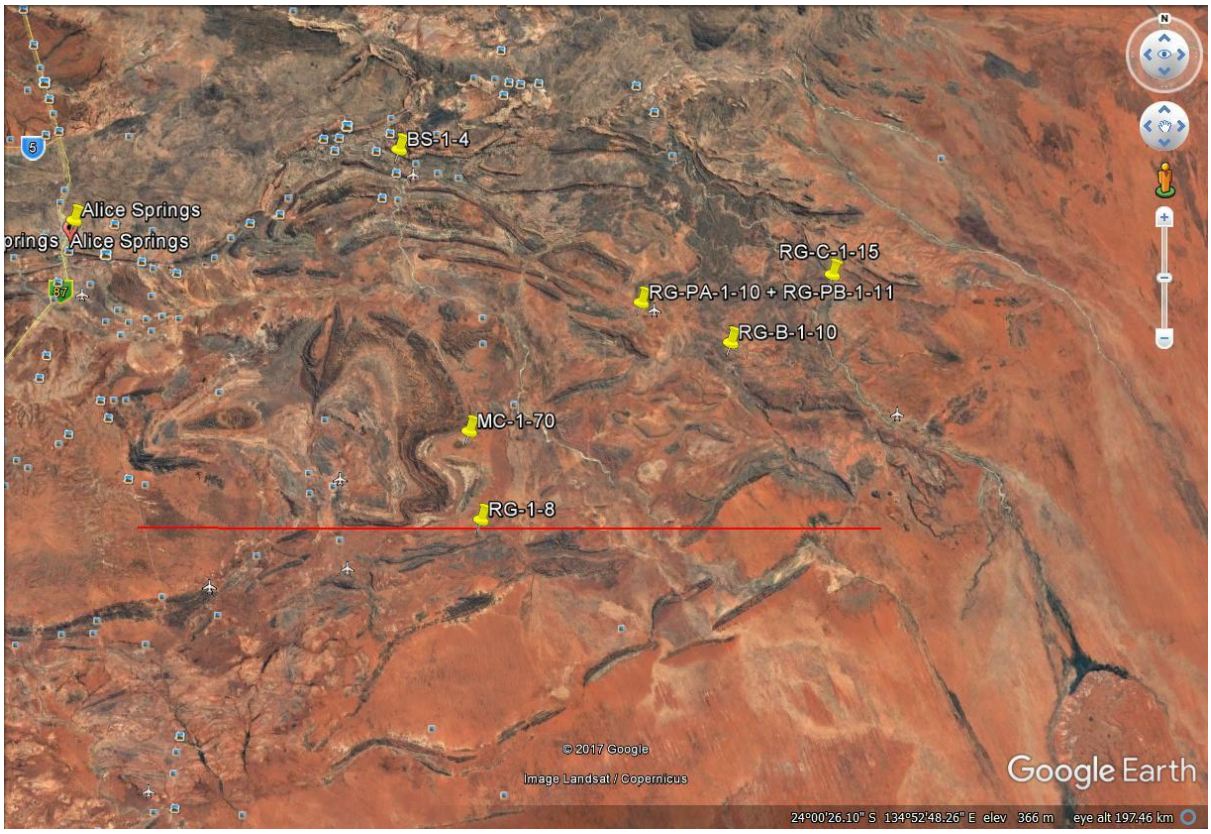

Close up view of the sampling sites, see table below for full locations.

Samples collected in 2017	Basic lithology/notes	Stratigraphic nomenclature	Sample ID	High Resolution Sections	Lattitude	Longitude
25-Jun	Domal Stromatile	Loves Creek Formation	BS-1	N/A	23° 34' 40''	134° 29' 10''
	Laminar "carbonate mud"	Loves Creek Formation	BS-2	N/A		
	contact - laminar Dolitic sample	Loves Creek Formation	BS-3	N/A		
	Columnar stromatolite	Loves Creek Formation	BS-4	N/A		
26-Jun	On top of valley, stromatolites	Ringwood member	RG-1	N/A	24° 12' 5''	134° 38' 23''
	On top of valley, stromatolites	Ringwood member	RG-2	N/A		
	On top of valley, stromatolites	Ringwood member	RG-3	N/A		
	On top of valley, stromatolites	Ringwood member	RG-4	N/A		
	On base of valley, stromatolites	Ringwood member	RG-5	N/A	24° 12' 18''	134° 38' 27''
	On base of valley, stromatolites	Ringwood member	RG-6	N/A		
	On base of valley, stromatolites	Ringwood member	RG-7	N/A		
	Base of Ringwood oldest, stromatolites	Ringwood member	RG-8	N/A	24° 04' 24.9''	134° 42' 11.6''
27-Jun	Diamictite	Diamictite	MC-1	just below cap	24° 03' 19.1''	134° 37' 08.5''
	Cap Carbonate	Olympic Cap	MC-2	30cm		
	Cap Carbonate	Olympic Cap	MC-3	90cm		
	Cap Carbonate	Olympic Cap	MC-4	140cm		
	Cap Carbonate	Olympic Cap	MC-5	240cm		
	Cap Carbonate	Olympic Cap	MC-6	330cm		
	Cap Carbonate	Olympic Cap	MC-7	390cm		
	Cap Carbonate	Olympic Cap	MC-8	470cm		
	Cap Carbonate	Olympic Cap	MC-9	550cm	24° 03' 19.6''	134° 37' 0.85''
	Cap Carbonate	Olympic Cap	MC-10	550cm	24° 03' 19.5''	134° 37' 08.1''
	Cap Carbonate	Olympic Cap	MC-11	610cm		

Cap Carbonate	Olympic Cap	MC-12-A	680cm		
Cap Carbonate	Olympic Cap	MC-12-B	770cm		
Cap Carbonate	Olympic Cap	MC-13	970cm		
Cap Carbonate	Olympic Cap	MC-14	1020cm		
Cap Carbonate	Olympic Cap	MC-15	1000cm	24° 03' 19.8''	134° 37' 07.7''
Cap Carbonate	Olympic Cap	MC-16	1050cm		
Cap Carbonate	Olympic Cap	MC-17	1100cm		
Cap Carbonate	Olympic Cap	MC-18	1250cm		
Cap Carbonate	Olympic Cap	MC-19	1300cm		
Cap Carbonate	Olympic Cap	MC-20-A	1200cm		
Cap Carbonate	Olympic Cap	MC-20-B	1350cm		
Cap Carbonate	Olympic Cap	MC-21	1400cm		
Cap Carbonate	Olympic Cap	MC-22	1450cm		
Cap Carbonate	Olympic Cap	MC-23	1500cm		
Cap Carbonate	Olympic Cap	MC-24	1550cm		
Cap Carbonate	Olympic Cap	MC-25	1600cm		
Cap Carbonate	Olympic Cap	MC-26	1650cm		
Cap Carbonate	Olympic Cap	MC-27	1700cm		
Cap Carbonate	Olympic Cap	MC-28	1750cm		
Cap Carbonate	Olympic Cap	MC-29	1800cm		
Cap Carbonate	Olympic Cap	MC-30	1850cm		
Cap Carbonate	Olympic Cap	MC-31	1900cm		
Cap Carbonate	Olympic Cap	MC-32	1950cm		
Cap Carbonate	Olympic Cap	MC-33	2000cm		
Cap Carbonate	Olympic Cap	MC-34	2050cm		
Cap Carbonate	Olympic Cap	MC-35	2100cm		
Cap Carbonate	Olympic Cap	MC-36	2150cm		
Cap Carbonate	Olympic Cap	MC-37	2200cm		
Cap Carbonate	Olympic Cap	MC-38	2250cm		
Cap Carbonate	Olympic Cap	MC-39	2300cm		
Cap Carbonate	Olympic Cap	MC-40	2350cm		
Cap Carbonate	Olympic Cap	MC-41	2400cm		
Cap Carbonate	Olympic Cap	MC-42	2450cm		
Cap Carbonate	Olympic Cap	MC-43	2500cm		
Cap Carbonate	Olympic Cap	MC-44	2550cm		
Cap Carbonate	Olympic Cap	MC-45	2600cm		
Cap Carbonate	Olympic Cap	MC-46	2650cm		
Cap Carbonate	Olympic Cap	MC-47	2700cm		
Cap Carbonate	Olympic Cap	MC-48	2750cm		
Cap Carbonate	Olympic Cap	MC-49	2800cm		

	Cap Carbonate	Olympic Cap	MC-50	2850cm		
	Cap Carbonate	Olympic Cap	MC-51	2900cm		
	Cap Carbonate	Olympic Cap	MC-52	2950cm		
	Cap Carbonate	Olympic Cap	MC-53	3000cm		
	Cap Carbonate	Olympic Cap	MC-54	3025cm		
	Cap Carbonate	Olympic Cap	MC-55	3050cm		
	Cap Carbonate	Olympic Cap	MC-56	2075cm		
	Cap Carbonate	Olympic Cap	MC-57	3125cm		
	Cap Carbonate	Olympic Cap	MC-58	3150cm		
	Cap Carbonate	Olympic Cap	MC-59	3175cm		
	Cap Carbonate	Olympic Cap	MC-60	3200cm		
	Cap Carbonate	Olympic Cap	MC-61	3225cm		
	Cap Carbonate	Olympic Cap	MC-62	3300cm		
	Cap Carbonate	Olympic Cap	MC-63	3325cm		
	Cap Carbonate	Olympic Cap	MC-64	3350cm		
	Cap Carbonate	Olympic Cap	MC-65	3375cm		
	Cap Carbonate	Olympic Cap	MC-66	3400cm		
	Cap Carbonate	Olympic Cap	MC-67	3425cm		
	Cap Carbonate	Olympic Cap	MC-68	3450cm		
	Cap Carbonate	Olympic Cap	MC-69	3475cm		
	Cap Carbonate	Olympic Cap	MC-70	3500cm	24° 03' 07.7''	134° 37' 07.7''
		Pertatataka Formation	PT-1	just above cap		
28-Jun	laminar silty- carbonate mudstone	Ringwood member	RG-B-1	N/A	23° 49' 54.3''	134° 57' 25.7''
	laminar silty- carbonate mudstone	Ringwood member	RG-B-2	N/A		
	laminar silty- carbonate mudstone	Ringwood member	RG-B-3	N/A		
	laminar silty- carbonate mudstone	Ringwood member	RG-B-4	N/A		
	laminar silty- carbonate mudstone	Ringwood member	RG-B-5	N/A	23° 57' 47.3''	135° 06' 51.1''
	sandy limestone with cross beds	Ringwood member	RG-B-6	N/A	23° 57' 45.7''	135° 06' 42.5''
	sandy limestone with cross beds	Ringwood member	RG-B-7	N/A		
	stromatolites (domal)	Ringwood member	RG-B-8	N/A		
	stromatolites (domal)	Ringwood member	RG-B-9	N/A		
	stromatolite dome with sandy limestone	Ringwood member	RG-B-10	N/A		

29-Jun	first occurance of carbonate, just above diamictite	Ringwood member	RG-C-1	N/A	23° 47' 05.1''	135° 17' 29.1''
	finely laminated	Ringwood member	RG-C-2	N/A	23° 47' 06.9''	123° 17' 27.6''
	Ringwood	Ringwood member	RG-C-3	N/A	23° 47' 23.2''	135° 17' 26.5''
	dark grey massive	Ringwood member	RG-C-4	N/A	23° 47' 23.8''	135° 17' 24.5''
	Ringwood	Ringwood member	RG-C-5	N/A	23° 47' 35.0''	135° 17' 24.1''
	base of cliff	Ringwood member	RG-C-6	N/A	23° 48' 03.4''	135° 17' 43.6''
	first occurance of sandy limestone with cross beds	Ringwood member	RG-C-7	N/A	23° 48' 0.38''	135° 17' 45.0''
	finely laminated limestones below "stromatolite tubes"	Ringwood member	RG-C-8	N/A	23° 48' 04.8''	135° 17' 46.5''
	stromatolite "tube" above finely laminated	Ringwood member	RG-C-9	N/A	23° 48' 04.8''	135° 17' 46.5''
	top of first ridge in ringwood	Ringwood member	RG-C-10	N/A	23° 48' 06.7''	135°17' 47.3''
	stromatolitic layer	Ringwood member	RG-C-11	N/A	23° 48' 6.7''	135° 17' 47.3''
	columnar stromatolite	Ringwood member	RG-C-12	N/A	23° 48' 07.3''	135° 17' 52.3''
	just below top of ringwood,stromatolite occurances	Ringwood member	RG-C-13	N/A	23° 48' 19.1''	135° 18' 2.2''
	top of ringwood, limestone with cross beds	Ringwood member	RG-C-14	N/A	23° 48' 18.6''	135° 18' 4.4''
	total top of ringwood member, on top of ridge	Ringwood member	RG-C-15	N/A	23° 48' 18.9''	135° 18' 7.2''
	1st Cyclic profile	Ringwood member	RG-PA-1	0cm	23° 48' 16.5''	135° 17' 59.8''
	1st Cyclic profile	Ringwood member	RG-PA-2	20cm		
	1st Cyclic profile	Ringwood member	RG-PA-3	40cm		
	1st Cyclic profile	Ringwood member	RG-PA-4	60cm		
	1st Cyclic profile	Ringwood member	RG-PA-5	80cm		

1st Cyclic profile	Ringwood member	RG-PA-6	100cm
1st Cyclic profile	Ringwood member	RG-PA-7	120cm
1st Cyclic profile	Ringwood member	RG-PA-8	140cm
1st Cyclic profile	Ringwood member	RG-PA-9	160cm
1st Cyclic profile	Ringwood member	RG-PA-10	180cm
2nd Cyclic profile	Ringwood member	RG-PB-1	200cm
2nd Cyclic profile	Ringwood member	RG-PB-2	220cm
2nd Cyclic profile	Ringwood member	RG-PB-3	240cm
2nd Cyclic profile	Ringwood member	RG-PB-4	260cm
2nd Cyclic profile	Ringwood member	RG-PB-5	280cm
2nd Cyclic profile	Ringwood member	RG-PB-6	300cm
2nd Cyclic profile	Ringwood member	RG-PB-7	320cm
2nd Cyclic profile	Ringwood member	RG-PB-8	340cm
2nd Cyclic profile	Ringwood member	RG-PB-9	360cm
2nd Cyclic profile	Ringwood member	RG-PB-10	370cm
2nd Cyclic profile	Ringwood member	RG-PB-11	385cm

APPENDIX B: EXTENDED METHODS

All limestone samples were prepared through Prepfast, following Romaniello et al. (2015). In short 2 teflon vials are needed to process each sample- one for uptake and the other for sample collection. The automated process takes on average 24 hours to process 24 samples. See table below for summary of process for sample purification.

Table A1. Chromatographic steps for the automated separation of Sr by 1 mL ESI Sr–Ca column. Modified from Romaniello et al. (2015).

Step	Purpose	Volumn	Reagent
1	Condition column	10 mL	2 M HNO_3 + 1 wt% H_2O_2
2	Load sample	1 mL	2 M HNO_3
3	Elute sample matrix (not collected)	10 mL	2 M HNO_3 + 1 wt% H_2O_2
4	Elute Sr (collected)	6 mL	6M HNO_3
5	Elute Sr (not collected)	4 mL	6M HNO_3
6	Elute Ca (not collected)	10 mL	12 M HNO_3
7	Elute REEs, Hf, Cd, U and wash the column	10mL	1M HF

All Dolomite samples were prepared through standard column procedure below, following all required health and safety standards (see table below for process). A maximum of 20 samples were processed in one batch. After the sample are dried and ready to be loaded onto the filament for anaylsis.

Appendix 5. Sr Spec column procedure

User
Date

Sr column procedure	step completed (tick)
Remove columns from 3.5 M HNO3 storage container using blue PP forceps. Rinse 3 times with DI water and place in racks Load 200uL Sr Resin SPS (to column neck) using 1mL pipette. (Avoid bubbles in resin)	
Wash resin with 1 resevoir of 3.5M HNO3	
Wash resin with at least 2 resevoirs of DI H2O	
Equilibrate resin with 0.5mL 3.5M HNO3	
Load sample in 0.5mL 3.5M HNO3	
2 x wash with 0.6mL 3.5M HNO3	
2 x 0.5mL DI H2O - Collect Sr	
Add 1 drop 0.05M H3PO4 to Sr vial. (Also remember to spike any blanks)	
Add squirt (eg <1mL) of 15M HNO3 to oxidize any organics	
Dry on hot plate. (Lower temperatures towards dryness (~80C-100C) helps keep the 'Sr spot' desirably clear).	
Rinse columns 3 times using a pipette and DI H2O then return them to 3.5M HNO3 storage. (Rinse resin to waste container)	

Column #	Sample names
1	
2	
3	
4	
5	
6	
7	
8	
9	
10	
11	
12	
13	
14	
15	
16	
17	
18	
19	
20	
21	
22	
23	
24	
25	
26	
27	
28	
29	
30	

TIMS ANAYLSES

All filaments were welded and then degassed prior to analyses.

For each sample, the loading process was as follows;

The solutions were dropped on parafilm before pipetting and loading.
And the loading process was;

Centre filaments with non-zone-refined Re ribbon were used, no inner or outer filaments were used.

1. Load 1 μL 1M H_3PO_4 and evaporate at 0.5-0.8 A.

2. Load 0.5 μL Bircks Solution and evaporate at 0.5 A.

3. Load ~500ng Sr in 1 μL Bircks Solution and dry st 0.5 A.

4. Gradually increase to ~1 A, but reduce current if load starts to spread

5. Over about 1 minute, increase to 1.8 A and leave for 1 minute.

6. Heat to just red for several seconds, estimated at ~2.3-2.4 A.

7. Turn down the current

Following samples were loaded onto the magazine ready to analyses.

APPENDIX C: GEOCHEMICAL DATA

Trace and Major Elements (ppm)																
Sample Name	Na	Al	P	K	Sc	Cr	Mn	Fe	Ni	Cu	Zn	Rb	Sr	Zr	Cs	Ba
RG-PA-1	1381.0016	24770.7517	314.8808	6939.2385	8.5931	100.8125	2030.1880	93219.7729	5508.0459	55.7324	786.8449	26.6183	63.5194	1.3398	0.6995	2.7454
RG-PA-2	643.5762	10984.8173	193.6321	2222.8437	5.3532	27.6434	505.7537	32051.2815	84.0988	11.2101	408.0950	10.1212	83.2612	0.9190	0.2209	0.3003
RG-PA-3	2373.0703	23459.6033	213.4098	7411.3569	10.3663	44.6210	459.5632	73107.6906	67.9308	12.2545	448.3161	26.9466	231.9853	1.4531	0.3822	2.8480
RG-PA-4	1101.3772	14952.4006	121.9569	3790.9994	6.0915	30.1518	1202.4585	46863.9572	99.6608	8.7009	380.6186	13.6911	52.3907	1.0356	0.3014	2.5051
RG-PA-5	1296.4712	23561.6014	288.1459	6766.7259	9.1429	57.3312	85.0864	75717.0561	46.6160	15.6043	458.9055	26.1288	83.8892	0.9669	0.6371	11.6407
RG-PA-6	612.8071	6978.2958	105.4917	1042.3749	6.6904	26.6215	479.6504	18632.6763	7.0098	3.8466	85.8905	4.2711	98.3755	0.9997	0.0910	0.4432
RG-PA-7	1242.7248	12083.4801	239.6312	2627.9611	7.9835	37.5950	604.0874	32941.2468	28.9502	6.8242	223.2714	9.7620	120.5535	2.7741	0.3830	0.4658
RG-PA-8	977.6715	9912.8533	159.3092	2180.4882	7.2461	31.3766	1003.7848	29449.4755	17.9369	7.0142	257.6871	9.1854	176.0255	0.9432	0.3550	0.9498
RG-PA-9	1383.0405	13007.6240	299.2622	3787.3588	6.0072	33.6679	327.5700	37109.6179	26.6315	8.8089	255.1263	13.1679	58.6464	1.5302	0.4389	1.3546
RG-PA-10	1282.0314	10018.8105	324.2316	3074.0088	5.6649	25.9728	1141.0646	28843.6883	27.8478	8.1298	234.7746	9.4661	76.0850	2.3684	0.1328	8.8766
RG-PB-1	2201.0562	24056.0888	116.9303	6887.6057	10.4282	57.8808	858.2170	82718.8777	36.6299	4251.1303	1252.3915	26.1537	69.6305	1.0329	0.8184	1.4198
RG-PB-2	2952.0678	51898.2169	384.0555	16172.7819	18.0079	103.1597	253.0004	#########	64.2429	2433.5820	1077.2166	61.8740	47.1695	1.8146	2.2452	5.3244
RG-PB-3	2921.6020	43974.8205	385.3440	13010.0533	13.3392	113.0354	265.8999	#########	83.6899	2027.6889	809.1719	48.1416	50.1537	0.4339	1.0738	5.7387
RG-PB-4	1425.4382	15414.0685	349.7667	4052.0149	3.9014	43.2074	178.4318	57744.4336	21.8495	2169.2860	656.9391	15.4066	51.3721	0.5814	0.2948	1.3767
RG-PB-5	2737.4044	23996.3540	180.0150	6815.3030	8.2385	89.4541	2095.0696	82822.4852	801.7826	599.1589	261.7943	27.3129	91.6687	0.3291	0.4723	1.3186
RG-PB-6	2538.7875	28454.5221	281.1217	10169.7778	9.8433	168.6576	483.5826	#########	1071.5186	24.1318	132.1462	42.0689	95.2241	0.4221	0.7179	1.0945
RG-PB-7	2853.0208	34324.5230	682.6844	9879.8133	12.6252	82.4435	408.9783	97641.8809	63.3048	18.1953	142.2971	39.1357	115.3037	1.1395	0.5372	8.1271
RG-PB-8	521.0958	4397.1348	286.5084	923.9508	2.1234	23.9525	1398.7945	12252.1724	1139.9143	48.2397	423.1463	4.2664	132.1007	0.4618	0.1006	3.2993
RG-PB-9	1051.6168	9749.5619	160.4711	2600.0176	5.8868	59.6744	1460.9445	34756.8730	537.7218	9.7043	70.3058	10.5256	89.1420	0.5693	0.2250	2.5901
RG-PB-10	1860.1199	18172.3730	832.6140	4398.9005	8.5420	75.3361	1672.5075	51834.2712	297.0023	21.6637	682.8301	15.9465	48.8865	0.6409	0.3417	7.0077
RG-PB-11	1112.0992	9102.8655	148.3124	1958.0497	6.4936	27.2975	128.7741	22223.6387	22.8092	7.8863	59.3139	7.0754	181.4320	0.5697	0.1095	1.3815
RG-C-1	183.8593	803.2378	113.2427	159.5743	1.4835	2.6044	1502.6611	5294.8716	13.2995	1.1438	96.6740	0.9102	72.9981	0.1310	#VALUE!	0.0354
RG-C-2	279.3860	3264.9404	133.5285	417.3075	3.2758	6.0017	2058.6556	13068.5281	7.1464	2.5057	265.0032	1.9736	116.8969	0.3371	0.0454	90.9176
RG-C-4	455.1165	9154.7888	199.7862	1196.1554	5.7407	15.0130	9820.2780	34428.5451	138.5164	4.9295	48.2706	5.1858	309.2497	0.1136	0.0591	1.4658
RG-C-5	822.1338	18666.8821	354.3515	4800.3403	6.2897	30.2612	490.6089	63729.6016	62.4601	16.6185	225.3439	17.2835	45.6293	0.2584	0.3314	4.9904

RG-C-6	1227.5935	12408.5889	179.0041	2459.9668	7.9067	36.8651	651.9657	39422.7478	100.0934	7.6832	107.9500	10.4637	325.3168	0.2712	0.1786	10.0707
RG-C-7	311.1389	3809.9078	111.5356	570.9946	5.2458	16.2905	6930.8880	66398.4385	224.0540	3.1597	104.4469	2.5896	228.2540	0.0519	0.0824	0.4394
RG-C-8	758.6386	14277.6294	309.0654	2838.7300	6.4861	29.8568	98.5732	41848.5658	69.0108	7.8548	139.5648	11.0484	105.6184	0.3772	0.1317	1.9557
RG-C-9	86.0207	275.3038	39.6777	101.9445	0.9759	1.9549	1804.5108	19181.0927	7.6234	0.3098	43.1219	0.4805	372.4080	0.0359	0.0229	0.7511
RG-C-10	209.6146	1616.6269	107.5061	307.9366	3.6482	5.0823	1014.1608	12932.7737	8.5413	0.9424	31.4091	1.5510	463.3952	0.1215	0.0865	0.5794
RG-C-11	278.6617	1775.4209	105.5286	273.8172	4.4910	8.1423	494.6583	8429.1326	7.6520	2.0003	32.0189	1.2909	345.3544	0.1049	0.0357	0.8865
RG-C-12	95.3072	577.9694	72.5845	103.3403	1.3193	2.3554	772.7805	13351.5852	2.3327	0.3303	20.9525	0.5145	362.8479	0.1498	0.0484	0.1924
RG-C-13	89.8823	429.9410	77.7806	104.2267	1.3239	1.5300	467.5248	4316.3999	0.6525	0.5939	26.1906	0.4883	303.1555	0.0696	0.0358	0.5682
RG-C-14	180.7013	1260.6062	98.1946	278.2957	3.1941	6.3978	208.0607	10290.0675	10.5705	2.5524	36.8405	1.3646	533.1360	0.0803	0.0976	0.3063
RG-C-15	70.1126	658.0211	47.4492	132.7089	1.4432	1.8627	119.2387	4440.5779	1.4192	1.1485	16.6393	0.5715	202.5383	0.0837	0.0283	0.5106
BS-1	23.7664	110.2284	33.3071	40.2187	0.2428	0.7786	98.6192	560.3855	2.7922	1.0434	14.7304	0.1735	59.8425	0.0404	0.0403	2.5684
BS-2	47.9739	257.1302	53.5098	133.6593	0.4767	2.2586	80.3582	2167.0205	4.1464	0.6114	17.1078	0.4969	35.8363	0.0832	0.0295	0.2344
BS-3	16.4940	120.8223	37.7813	37.4932	0.1503	0.8743	28.2196	453.2067	0.9291	1.1269	25.9024	0.1905	31.3915	0.0322	0.0295	0.0837
BS-4	62.4543	408.1349	123.0456	124.4279	0.5751	1.4626	106.8677	728.7611	3.9351	1.8366	277.7635	0.7510	53.7269	0.0266	0.0469	4.6570
MC-2	90.0249	3307.7770	37.5266	697.4405	3.3779	4.3439	1246.0922	24290.2168	7.7681	1.9970	70.8439	2.9528	44.5977	0.4801	0.0669	0.0489
MC-4	137.3902	2395.4216	104.7513	591.2216	3.4998	5.1297	1093.6720	17829.1992	13.5082	21.2415	1089.8741	2.9105	65.7063	0.2159	0.1341	6.5885
MC-9	84.8800	3268.8000	52.4180	851.6813	3.1805	18.7875	762.3571	19040.0276	29.3622	20.0322	193.4078	3.5201	37.6646	0.3674	0.1001	0.5639
MC-10	107.1635	1717.0911	87.2776	383.7713	3.4104	5.0053	905.0337	15760.2721	22.8314	6.6767	255.4951	1.8673	58.4694	0.2407	0.1251	0.9598
MC-11	97.4885	1198.4744	73.2218	569.3060	2.1992	8.3991	351.8625	8491.2710	13.7702	6.3237	126.5306	2.6261	43.0153	0.3371	0.1047	0.3341
MC-12-A	84.7159	1996.3288	37.5465	273.1400	2.0406	2.4028	1439.2639	9512.2509	8.7437	4.1183	367.6868	2.0528	65.5088	0.2097	0.0637	0.0487
MC-12-B	84.7844	902.2393	123.6364	212.4235	3.4737	3.4112	667.0455	15479.9012	2.9730	2.6973	120.0663	1.2200	51.1579	0.4387	0.0867	330.7828
MC-13	73.7233	2686.2265	24.9151	537.3490	3.6783	2.1186	621.6597	21049.8813	8.1641	3.3696	109.8219	2.9606	56.2931	0.2435	0.0955	1.1230
MC-14	61.9749	883.4168	31.0254	164.0986	0.8744	1.7432	405.6089	7369.7793	9.2844	2.1258	205.2893	0.9385	37.4731	0.1003	0.0414	0.2692
MC-15	77.9587	1345.0282	39.8335	259.6812	1.5995	2.4265	431.4353	10937.3339	7.8826	4.4956	250.1233	1.5329	51.0949	0.3027	0.0569	1.8756
MC-16	70.4017	899.5000	25.4087	176.8342	1.6096	1.2872	483.9516	8999.1089	4.6245	2.6026	103.5855	0.8904	34.5693	0.1656	0.0305	0.1152
MC-17	80.5169	1648.2062	23.8440	539.2508	3.6197	2.5717	538.3770	16859.4260	3.5448	1.6448	138.1703	2.3446	51.9876	0.2325	0.0593	0.2914
MC-18	48.0562	1730.3634	21.2398	377.6002	2.3485	1.5678	669.7298	13651.9344	5.7045	2.0594	124.3554	1.7167	40.4985	0.1010	0.0392	0.4350
MC-19	64.8395	1447.5029	29.5647	456.2623	1.8887	2.0530	670.5666	14183.8491	4.9108	2.3970	143.1831	1.8777	49.8758	0.1777	0.0489	0.1597
MC-20-A	56.8429	1625.0141	30.5028	414.2248	2.5364	2.2827	524.0854	13872.6058	3.2835	1.9659	130.4146	1.8578	42.7573	0.2013	0.0433	0.1195

MC-20-B	72.8477	917.0080	49.2010	227.7426	1.3962	1.7366	567.4246	9906.6564	6.1434	3.6825	122.5003	1.1522	47.2976	0.3099	0.0398	1.4264
MC-21	74.0976	1512.3159	28.4316	368.0560	2.6891	1.4747	523.1444	11989.0684	7.7757	2.5910	101.5112	1.6231	40.2192	0.1401	0.0330	1.0840
MC-22	51.1339	1799.8029	21.9471	539.8035	1.7554	1.5101	503.7407	10306.2222	4.4719	1.7422	125.3775	2.3860	33.9607	0.1019	0.0419	2.7388
MC-23	57.1018	1859.7467	25.4663	627.9705	2.5705	1.9768	542.6732	13949.5032	9.8762	1.7624	108.1018	2.3628	43.4327	0.1715	0.0496	0.0938
MC-24	45.4935	746.4612	18.8575	231.4259	1.3078	1.4575	487.2780	8944.2631	5.5273	1.7753	12.2211	1.0523	35.3634	0.0704	0.0201	0.7138
MC-25	73.2537	1265.0604	26.6378	511.6563	2.2790	2.6288	577.5758	13649.7813	29.9614	2.3975	19.2915	1.8799	44.5447	0.1185	0.0225	0.6561
MC-26	54.8258	1305.7735	43.2009	263.6023	2.0138	1.7690	544.5677	12335.9574	13.0936	2.7686	18.3244	1.3371	48.4452	0.1404	0.0254	0.5318
MC-27	69.9860	2367.9895	92.8947	528.3677	2.5368	1.4393	458.9248	13353.8406	5.3184	2.3408	37.3035	2.1236	37.2504	0.1266	0.0275	0.3763
MC-28	52.3876	1647.6520	48.6317	430.8313	2.8595	1.7292	575.0591	11076.1974	3.3225	1.4124	37.5168	1.6716	31.9945	0.0714	0.0274	4.6264
MC-29	50.2667	1829.8007	58.1085	382.2077	2.5070	2.4631	575.4121	11575.0891	22.0518	2.1974	43.0236	1.3636	36.6241	0.0537	0.0225	0.0914
MC-30	57.7464	1457.5412	73.8450	329.3871	1.7689	2.4547	465.5152	10896.6186	20.8387	2.0552	45.7855	1.3170	34.8952	0.0787	#VALUE!	0.3517
MC-31	69.2309	2045.1234	62.2797	586.5738	3.3840	2.0975	661.6481	11600.1646	4.6107	1.6368	47.3163	2.3219	33.4338	0.0980	0.0342	0.3345
MC-32	63.4682	2488.4729	60.6399	731.2571	3.0932	1.8234	671.7398	13951.2700	8.7996	1.7966	45.1851	2.6558	38.9003	0.0927	0.0234	0.1859
MC-33	71.5291	1765.7927	116.1182	522.3057	2.6208	3.4423	678.3159	11232.9094	17.8014	2.6880	224.6336	2.0356	44.7894	0.0234	0.0305	0.1507
MC-34	51.4137	1845.4929	52.3123	393.4333	2.4927	1.3623	661.9001	9231.9052	12.6937	2.4459	70.3016	1.4386	42.0048	0.0825	0.0215	0.1254
MC-35	63.9815	1972.8099	53.4784	533.9373	2.1018	1.7989	947.3363	9400.7169	10.5350	2.4492	71.9375	2.1183	50.4015	0.0916	0.0331	0.2643
MC-36	111.2658	4741.3712	86.7562	1421.3782	5.4729	6.5123	374.1673	11737.0936	3.8316	1.8012	83.1103	4.8589	32.8296	0.2457	0.0793	0.2188
MC-37	72.0379	1900.1406	54.0900	671.3267	3.0603	1.1446	723.7090	10135.4826	7.3149	2.2107	76.9403	2.3730	50.0675	0.1535	0.0250	0.3325
MC-38	73.1792	1993.9411	75.5291	525.3536	2.7033	0.9418	600.6302	8961.0567	8.8908	2.2917	158.6601	2.1488	44.3540	0.0862	0.0329	#VALUE!
MC-39	73.2500	1787.4907	63.1972	423.4920	2.5219	0.8422	709.8406	6071.8489	4.9763	1.6493	111.5547	1.7028	53.2311	0.0600	0.0322	303.6220
MC-40	85.0107	1935.6596	72.3859	590.7202	2.2410	1.8690	894.5539	9046.3077	15.4506	1.9211	121.0160	2.4103	43.2171	0.0905	0.0403	0.1080
MC-41	83.5442	3277.7361	57.7441	536.2920	5.3399	1.5653	774.9609	9999.5028	5.8784	2.3872	123.8713	1.8249	41.8274	0.0743	0.0326	2.6492
MC-42	92.2563	2502.7635	73.9122	282.3722	4.4717	1.3031	838.2923	8776.2660	6.3695	2.2748	128.6889	1.3743	50.0753	0.0857	0.0383	0.3940
MC-43	121.2523	3394.6525	81.2621	675.5878	7.5633	3.8045	814.8224	9924.0525	5.0549	3.3493	135.7434	2.4961	43.2074	0.1232	0.0796	0.1269
MC-44	204.4433	6368.4176	135.7326	1660.8918	8.6766	4.6856	521.1892	14361.7077	11.2281	6.6313	545.6845	6.1031	57.4364	0.0731	0.1266	0.3854
MC-45	125.3727	4247.1619	98.5250	853.7563	6.0925	2.5879	712.8204	10733.5590	6.6452	4.8922	262.7423	3.5295	33.7395	0.0795	0.0934	0.2119
MC-46	68.4129	2578.7356	118.4697	435.8523	2.1496	1.4642	708.8737	8336.0548	7.1991	2.9598	303.8111	2.2528	31.8202	0.0247	0.0474	0.3404
MC-47	81.8862	4073.4622	95.9996	735.8272	3.7795	1.5708	800.3554	13422.4643	8.2806	3.4480	250.1094	2.9272	41.8188	0.0396	0.0373	0.1614
MC-48	90.1396	3843.5456	95.1675	933.9874	5.6461	1.8175	748.2295	13204.4794	7.0588	5.9954	241.9100	3.7294	42.5070	0.0487	0.0585	0.3820

MC-49	95.6969	3196.2171	115.2350	853.1663	4.4510	2.0497	974.5028	15870.4218	7.2392	3.2820	267.7268	3.1802	45.3975	0.0498	0.0410	0.2291
MC-50	91.0973	3230.8768	121.0817	764.9670	3.1527	2.4461	1245.5858	15297.6311	6.7348	3.1293	246.7774	3.0790	48.1902	0.0382	0.0378	0.2076
MC-51	91.8529	4626.7533	100.9418	887.8146	5.1746	2.0652	871.2594	21107.9642	13.0606	4.1861	299.8408	3.7695	46.6315	0.0357	0.0571	1.4113
MC-52	79.5781	4370.2633	39.8397	894.0563	5.5166	1.1508	985.1212	18655.9711	7.2670	2.7992	52.3635	3.0969	42.9943	0.1147	#VALUE!	2.7591
MC-53	43.8236	1858.2175	55.2917	433.7922	1.8280	1.3482	1300.4316	18061.7707	9.6721	2.3832	44.5672	2.0593	38.3319	0.0842	#VALUE!	1.5728
MC-54	61.4678	2249.2443	57.4298	520.9234	2.2598	2.0009	714.1828	20268.4802	5.9002	2.4272	50.8975	2.3881	46.3179	0.1429	#VALUE!	8.1128
MC-55	39.7927	1003.9192	80.5618	238.8201	1.0048	0.9823	1014.9974	14840.1305	5.1278	4.8640	46.4168	1.1098	45.3756	0.0608	#VALUE!	3.6293
MC-56	51.7581	1695.1600	61.4745	369.1388	1.7888	2.5249	1108.7391	21573.0520	7.7322	4.1121	51.2371	1.8533	43.3186	0.1018	0.0291	4.9105
MC-57	47.8567	1041.5725	111.1962	272.3994	1.5231	1.0270	1451.1773	12364.4068	7.2091	3.5008	26.1574	1.4616	43.5852	0.1093	0.0253	0.0408
MC-58	34.1238	2395.7059	47.4714	497.5872	2.7807	1.5029	864.8513	15611.6997	3.3961	2.9893	30.5019	2.3391	33.4327	0.1029	0.0292	94.8000
MC-59	65.3038	4107.9662	60.7183	813.1110	4.3291	2.5332	1530.1013	16744.7277	4.7195	3.7102	42.2447	3.7715	41.7044	0.1725	0.0463	2.3984
MC-60	60.3898	667.1058	120.3194	170.6685	2.5101	#VALUE!	740.0449	3534.6413	2.3945	2.5291	24.1048	0.8345	54.6502	0.2107	#VALUE!	0.8167
MC-61	88.3671	5464.9413	43.7827	1240.1198	6.1623	3.3669	1289.9287	20323.2898	7.6119	4.0372	41.5176	5.6451	51.3202	0.2075	0.0617	0.9669
MC-62	66.8135	5361.8867	63.0747	1081.9462	5.3513	3.2001	1134.2195	16123.6872	8.2557	4.3377	42.2214	4.8870	59.4919	0.1649	0.0980	0.7730
MC-63	42.2883	2296.2193	104.2703	569.4583	5.1241	#VALUE!	1056.1388	12502.8961	4.2915	3.2347	27.0973	2.6149	67.3465	0.1214	#VALUE!	0.6515
MC-64	26.2165	1008.1783	97.2162	197.5771	4.1326	#VALUE!	1439.0115	7676.4982	4.0090	3.9083	26.8531	1.0359	68.7925	0.1388	#VALUE!	0.7037
MC-65	27.7997	1880.4053	186.5892	368.0778	4.7120	2.8352	307.3530	12284.3656	4.8447	4.8168	51.7879	1.9377	67.9818	0.1313	#VALUE!	0.7189
MC-66	40.7018	1325.5365	204.1070	176.7550	1.1548	1.5845	912.3778	5304.4938	2.2314	16.1271	29.8540	0.8156	68.7948	0.0768	0.0218	0.2040
MC-67	35.1384	857.5820	259.9719	138.8458	0.8855	1.6923	694.1771	3596.0726	2.8234	12.7589	24.2583	0.6805	85.1810	0.0858	#VALUE!	1.5457
MC-68	36.6010	2216.3205	134.1908	211.5820	1.1112	1.6897	916.9171	3414.6705	12.2405	13.4475	26.8083	0.8504	64.5117	0.0564	#VALUE!	2.7257
MC-69	56.0047	967.9428	190.1213	254.2348	0.6926	1.7821	628.1125	2592.4824	10.6457	54.8553	34.5989	1.0579	52.0675	0.1637	0.0146	15.0785
MC-70	56.2737	1336.2787	90.6160	277.6235	1.9635	2.4627	67867.4778	4873.4208	44.9226	16.3930	280.1247	1.3453	54.7972	0.0205	0.0235	0.5384
PT	4316.4146	73741.6494	2975.8907	17049.5098	13.3356	2153.8598	8.3406	83338.2337	7949.0531	68.7184	7880.3735	71.6641	157.3394	0.4400	0.9566	256.6590

Sample Name	La	Ce	Pr	Nd	Df	Eu	Gd	Tb	Dy	Y	Ho	Er	Tm	Yb	Lu	Ce*	pr *
RG-PA-2	7.1465	16.9500	2.4385	9.8698	2.3634	0.5556	2.4049	0.3467	1.9916	10.0858	0.3537	1.0112	0.1274	0.7356	0.1112	0.9171	1.0532
RG-PA-3	16.5127	35.0350	4.7653	19.3680	4.2765	0.9523	4.1992	0.6546	3.6176	18.5412	0.6526	1.6985	0.2361	1.4172	0.2339	0.9030	1.0265
RG-PA-6	12.7414	28.9552	3.5467	13.3796	2.6687	0.5560	2.5115	0.4281	2.1198	11.1246	0.3944	1.0623	0.1446	0.8823	0.1125	0.9865	1.0217
RG-PA-8	8.4673	21.5704	3.5486	14.1051	3.4886	0.9014	3.5707	0.6982	3.0092	15.1143	0.7048	1.4631	0.3354	1.1952	0.3004	0.8676	1.1225
RG-PA-10	7.5093	18.5885	2.5316	10.1264	2.2996	0.5460	2.2779	0.3685	2.0194	9.4338	0.3912	0.9700	0.1464	0.7623	0.1414	0.9640	1.0366
RG-PB-2	16.8072	35.3378	5.7353	20.0583	5.1003	1.9130	5.8729	1.6475	4.4144	18.3526	1.6025	2.5974	1.1007	1.9865	1.0050	0.8130	1.2062
RG-PB-3	14.0422	30.5045	4.1396	16.7993	3.8736	0.7253	3.8367	0.6019	2.9806	14.8038	0.5863	1.4498	0.1898	0.9107	0.1263	0.9137	1.0264
RG-PB-4	6.9283	16.4329	2.2920	9.7764	2.3644	0.4382	2.1774	0.3390	1.8209	9.1759	0.3030	0.8246	0.1070	0.6232	0.0783	0.9340	1.0081
RG-PB-5	10.8441	26.6696	3.2390	13.0675	2.8400	0.6417	2.9760	0.4512	2.6905	13.5889	0.4996	1.3490	0.1693	1.0690	0.1571	1.0268	0.9813
RG-PB-6	10.5469	23.2769	3.0745	12.2745	2.7780	0.6031	2.6859	0.3859	2.4656	12.6106	0.4827	1.2207	0.1573	1.0122	0.1611	0.9341	1.0243
RG-PB-7	20.2241	53.2813	7.0076	29.2266	6.9349	1.4741	6.7371	1.1118	5.5798	27.9688	1.0268	2.6814	0.3395	2.0327	0.2790	1.0094	0.9971
RG-PB-9	4.8902	11.9792	1.7701	7.2639	1.6338	0.3938	1.6820	0.2629	1.4860	7.7114	0.3139	0.7357	0.1056	0.5545	0.0848	0.9142	1.0558
RG-PB-10	25.6386	70.7041	9.2918	38.4821	9.1571	2.2666	9.2068	1.4220	7.8484	39.0157	1.4799	3.4106	0.4885	2.4593	0.4541	1.0284	1.0008
RG-PB-11	8.8678	21.6575	3.2090	13.3231	3.2887	0.7502	3.2003	0.5077	2.6521	12.7686	0.4797	1.1446	0.1868	0.9557	0.1613	0.9116	1.0496
RG-C-1	3.4210	7.5479	1.0329	4.0903	1.1621	0.3718	1.4407	0.2435	1.3506	7.1201	0.2456	0.5879	0.0761	0.4262	0.0688	0.9156	1.0447
RG-C-6	30.9295	58.4045	6.9437	25.0339	4.8568	1.0714	4.7787	0.6610	3.4226	16.9576	0.5967	1.5628	0.2074	1.1278	0.1902	0.9159	1.0318
RG-C-10	13.6943	27.9999	3.2198	12.1303	2.6209	0.7046	2.8648	0.4966	2.5832	14.6959	0.5296	1.3260	0.2112	1.0174	0.2000	0.9693	0.9924
RG-C-12	9.4273	19.7429	2.1697	7.9824	1.7967	0.4837	1.9131	0.3333	1.8245	11.3084	0.3664	0.9462	0.1344	0.6682	0.1125	1.0035	0.9825
RG-C-13	5.7743	10.8657	1.2067	4.1224	0.7883	0.1957	0.8300	0.1512	0.8437	5.8429	0.1970	0.5324	0.0839	0.4032	0.0733	0.9447	1.0247
RG-C-14	8.2102	17.7010	2.0337	7.3163	1.6412	0.3811	1.6246	0.3177	1.7804	10.7946	0.4007	1.0306	0.1738	0.9130	0.1515	0.9954	1.0158
RG-C-15	3.3402	6.9136	0.7914	2.8449	0.5488	0.1363	0.6080	0.1154	0.6142	3.6518	0.1402	0.3748	0.0581	0.2896	0.0542	0.9775	1.0143
MC-2	2.3602	7.5142	1.1922	5.7240	1.7157	0.3969	1.7242	0.2823	1.4693	7.8000	0.2788	0.6986	0.0906	0.4732	0.0844	0.9581	0.9821
MC-4	2.9020	9.2479	1.4475	7.1088	2.0992	0.4421	2.0426	0.3018	1.6200	8.4767	0.3146	0.7766	0.1131	0.4879	0.0834	0.9673	0.9631
MC-9	1.7018	5.4232	0.8156	3.9254	1.1580	0.2512	1.0892	0.1737	0.8571	4.4463	0.1701	0.4248	0.0701	0.2810	0.0560	0.9938	0.9623
MC-10	2.3802	7.6518	1.2813	7.1165	2.2703	0.4733	2.0351	0.2868	1.5343	7.9621	0.2863	0.6738	0.1013	0.5092	0.0964	0.9259	0.9053
MC-12-A	1.8088	6.5203	1.0126	5.8523	1.9340	0.4019	1.7221	0.2488	1.3267	7.4063	0.2456	0.6135	0.0783	0.4031	0.0636	1.0101	0.8607
MC-15	1.6186	6.2427	1.0274	5.6115	1.5291	0.2769	1.2188	0.1837	0.9388	5.3605	0.1788	0.4373	0.0595	0.3369	0.0480	0.9875	0.9112

MC-17	1.7920	6.7970	0.9544	5.0540	1.4004	0.2812	1.2930	0.1868	1.0346	5.8822	0.2033	0.5177	0.0632	0.3711	0.0613	1.1006	0.8830
MC-20-B	1.8301	6.1770	1.1426	6.5648	2.0793	0.3927	1.7006	0.2689	1.3518	8.1209	0.2714	0.6803	0.0873	0.4751	0.0684	0.8747	0.9093
MC-25	1.9965	6.1156	0.9729	5.7010	1.9025	0.3628	1.6676	0.2456	1.3317	8.0492	0.2577	0.6517	0.0864	0.4734	0.0718	0.9446	0.8587
MC-30	1.2921	4.3291	0.7038	4.1581	1.4704	0.3076	1.2937	0.1958	0.9808	5.6637	0.1844	0.4653	0.0638	0.3063	0.0512	0.9571	0.8593
MC-32	1.5487	5.7491	0.8196	4.6502	1.8269	0.3467	1.5836	0.2399	1.2435	7.0996	0.2429	0.6038	0.0783	0.4440	0.0673	1.0819	0.8480
MC-39	0.9169	2.7196	0.4239	2.4921	1.1340	0.2451	1.0934	0.1849	0.9024	4.6121	0.1819	0.4559	0.0691	0.3352	0.0545	0.9476	0.8514
MC-44	3.4070	16.4542	1.3287	6.6487	2.5307	0.5383	2.4671	0.3704	1.9589	11.0551	0.4015	1.0033	0.1469	0.7695	0.1212	1.7215	0.7222
MC-48	1.7054	5.6817	0.6785	3.5629	1.6225	0.3567	1.6552	0.2704	1.4472	8.3063	0.2944	0.7865	0.1144	0.6427	0.1033	1.1728	0.8360
MC-51	1.7359	5.5062	0.7696	4.3056	1.9023	0.4414	1.9448	0.3024	1.8255	10.9089	0.3804	1.0411	0.1422	0.8313	0.1405	1.0416	0.8504
MC-53	1.4083	4.7163	0.6245	3.7409	1.6393	0.3319	1.4919	0.2397	1.3323	8.6087	0.2540	0.6695	0.0844	0.4565	0.0648	1.0996	0.7981
MC-57	2.6780	9.1598	1.7113	10.1975	3.7336	0.7182	3.2735	0.4816	2.5032	17.3146	0.5019	1.2736	0.1724	0.9473	0.1379	0.8715	0.8878
MC-62	6.5502	17.0670	2.0542	9.1062	2.6005	0.5223	2.3662	0.4105	2.3385	14.6516	0.4967	1.2911	0.2035	1.0409	0.1660	1.0583	0.9271
MC-63	6.6330	18.6712	2.1509	9.7969	2.7836	0.6111	2.4351	0.3799	2.0326	12.8443	0.3926	1.0805	0.1399	0.6947	0.1249	1.1215	0.8958
MC-64	6.5905	18.9457	2.6480	13.1897	3.8943	0.7458	3.0282	0.4397	2.3875	14.7804	0.4514	1.1207	0.1489	0.7692	0.1117	1.0057	0.9169
MC-65	5.1900	11.1640	1.7483	8.6286	2.7337	0.5621	2.6183	0.3790	1.9194	12.7665	0.3559	0.9509	0.1229	0.6139	0.0927	0.8381	0.9601
MC-69	2.9745	6.3801	0.7324	2.9852	0.6265	0.1766	0.6530	0.1043	0.6017	4.8511	0.1219	0.3356	0.0460	0.2596	0.0343	0.9934	0.9511
MC-70	18.5300	2.1823	9.4804	2.4999	0.5594	2.0574	0.3055	1.4449	8.8470	0.2844	0.6865	0.0935	0.5382	0.0774	1.1413	0.9361	